

**Experimental Impacts into Chondritic Targets, Part I:
Disruption of an L6 Chondrite by Multiple Impacts**

Mark J. Cintala
Friedrich Hörz

Code KR
NASA Johnson Space Center
Houston, TX 77058

Submitted to *Meteoritics and Planetary Science*

Abstract

A fragment of an L6 chondrite (ALH 85017,13) with an initial mass (M_0) of 464.1 g was the target in a series of experimental impacts in which the largest remaining fragment (M_R) after each shot was impacted by a 3.18-mm ceramic sphere at a nominal speed of 2 km s^{-1} . This continued until the mass of the largest remaining piece was less than half the mass of the target presented to that shot (M_S). Two chunks of Bushveldt gabbro with similar initial masses were also impacted under the same conditions until M_R was less than half M_0 . The two gabbro targets required a total of 1.51×10^7 and $1.75 \times 10^7 \text{ erg g}^{-1}$ to attain 0.27 and 0.33 M_R/M_0 , respectively; the chondrite, however, was considerably tougher, reaching 0.40 and 0.21 M_R/M_0 only after receiving 2.37×10^7 and $3.10 \times 10^7 \text{ erg g}^{-1}$, respectively. The combined ejecta and spallation products from the gabbro impacts were coarser than those from the chondrite and in sufficient quantities that the new surface areas exceeded those from the meteorite until the fifth shot in the chondrite series, which was the number of impacts required to disrupt each gabbro target (*i.e.*, $M_R/M_0 \leq 0.5$). Unlike the behavior shown in previous regolith-evolution series, neither gabbro target produced an enhancement in the size fraction reflecting the mean size of the crystals composing the rock (about 3 mm), an effect possibly related to the width of the shock pulse. The original chondrite was so fine-grained and fractured, and the variance in its grain-size distribution so large, that effects related to grain-size were relegated to the $<63\text{-}\mu\text{m}$ fraction. Impacts into ALH 85017 produced abundant, fine-grained debris, but otherwise the slopes of its size distributions were comparable to those from other experiments involving natural and fabricated terrestrial targets. The characteristic slopes of the chondrite's size distributions, however, were notably more constant over the entire nine-impact series than those from any of the terrestrial targets, a testament to the control over comminution apparently exerted by pre-existing fractures and other, microscopic damage in the meteorite. The enhancement in the finer fraction of debris from ALH 85017 indicates that ordinary chondrites in solar orbit would be very efficient contributors to the cosmic-dust complex. At the same time, the greater resistance to disruption displayed by ordinary chondrites relative to that exhibited by igneous rocks indicates that a selection effect could be operative between the annealed, ordinary-chondritic breccias and relatively weaker, differentiated meteorites. Preferential survival from their time in the regoliths of their parent bodies through their transit to Earth and passage through the atmosphere suggests that meteorite collections could be biased in favor of the ordinary chondrites.

Introduction

The development and evolution of regoliths on undifferentiated asteroids as well as the evolution and fates of those asteroids themselves are dominated by the effects of impact. While it is easy to visualize the impact destruction of an asteroid fragment — whether in solar orbit after being ejected from the asteroid by a previous impact or as a substantial boulder in the asteroid's regolith — the details of the its disruption can be so complex as to seem intractable. Unlike the situation in which a single, energetic collision pulverizes that block, the much more common case of constant bombardment by very small, erosive micrometeoroids punctuated by the occasional larger impact complicates matters by changing the integrity, strength, mass, density, and porosity of the block with time. Even in the simpler case of the disruptive, isolated impact, the detailed effects of comminution depend to a great degree on the mineralogy, texture, and physical condition of the target materials, as has been demonstrated extensively through experimentation (*e.g.*, Matsui et al., 1982, 1984; Hörz et al. 1985; Cintala and Hörz 1990; Ryan et al., 1991, 1999; Cintala et al. 1993; Hörz and Cintala 1997; Housen and Holsapple 2003). All of those studies used terrestrial materials as targets which, aside from the obvious advantage of ready availability, afford a wide range of chemical, textural, and physical properties that could be varied as necessary to examine their specific effects on collisional outcomes. Asteroids are not composed of terrestrial rocks, however, and with spacecraft observations (Cheng and Barnouin-Jha 2003; Housen and Holsapple 2003) and numerical models (Asphaug et al. 1998) amassing more evidence that the collisional behaviors of asteroids and their regolith components are dependent on their physical properties, it is natural to question the suitability of using terrestrial materials to simulate asteroidal targets. With so little known about the physical response of asteroidal materials to impact, there is little basis for the selection of any particular terrestrial "analogue."

Accompanying the uncertainties in material behavior is the design of the disruption experiments themselves. Most conducted to date have been designed more to assess the impact strengths of different target materials than to simulate actual impact conditions involving asteroids or asteroid fragments. Although exceptions exist (*e.g.*, Gault and Wedekind 1969; Hörz et al. 1985; Ryan et al., 1991; Nakamura et al. 1992; Nakamura 1993), almost all impact-disruption experiments have used a single impact per target, typically either a sphere or a cube, with an impact parameter as close to zero as possible, which is clearly an idealized situation. (See the reviews of Cerroni [1986] and Fujiwara et al. [1989]; even more experiments have been conducted since then.) This approach provides the most tightly constrained conditions for evaluating the disruptive process, in that the impact geometry can be controlled and a target as pristine as possible can be used for each experiment, thus minimizing or eliminating complicating factors related to shock propagation and free-surface geometry. Natural collisions, on the other hand, occur over all values of the impact parameter thus including oblique angles, transferring energy to the

target very differently than in idealized single-impact experiments (*e.g.*, Gault 1973; Nakamura et al. 1992; Nakamura 1993; Benz and Asphaug 1994).

Destruction of an asteroid, meteoroid, or regolith fragment can also occur through the combined effects of impacts that cause small-scale surface "abrasion" through those large enough to induce instantaneous pulverization (*e.g.*, Gault et al. 1972; Hörz et al. 1974, 1975; Hörz 1977). It has been documented that, at least at laboratory scales, the total kinetic energy required to disrupt a given target is roughly constant regardless of whether that energy is delivered through a single collision or by multiple, smaller impacts (Gault and Wedekind 1969; Hörz et al. 1985). Differences in the products generated by these end members of the impact spectrum, however, can be considerable (Gault and Wedekind 1969; Hörz et al. 1985; Benz and Asphaug 1994).

Understanding the collisional evolution of asteroids, their surfaces, and their interiors will depend critically on information describing the behavior of asteroidal materials. Flynn and Durda (2004) have performed a number of single-impact disruption experiments on a variety of meteorite fragments, including a set of ordinary chondrites. Their results have shown that the ordinary chondrites are surprisingly tough targets, particularly in light of their polymict, brecciated natures. In an attempt to extend the dataset on ordinary chondrites to a multiple-impact context, we have performed experiments on an ordinary-chondrite target provided by the Johnson Space Center Meteorite Curator through the Meteorite Working Group. The overall purpose of this study was to document the physical and chemical changes as a solid meteorite fragment was reduced to a coarse "regolith" by repeated impact, an objective that was met in two distinct phases, each with its own experimental protocol. This paper describes the results of the initial segment of the project, in which the original meteorite fragment was disrupted by multiple impacts. A companion paper will treat the subsequent experiments in which all of the debris from the disrupted meteorite was collected to serve as a target for repetitive, "regolith-evolution" experiments.

The Target

The fragment allocated by the Meteorite Working Group, ALH 85017,13, was a 502.5-g piece (Fig. 1) of a larger L6 chondrite. It was a coherent block, with only shallow fracturing visible on the new surfaces that apparently was created when the piece was split from the parent mass. Some oxidation of iron particles was evident on all faces of the meteorite, particularly below the fusion crust (Fig. 1), and almost certainly derived from terrestrial weathering. These rust stains decreased in number and intensity as deeper parts of the meteorite were exposed during the experiments (as is visible in Fig. 2B), although

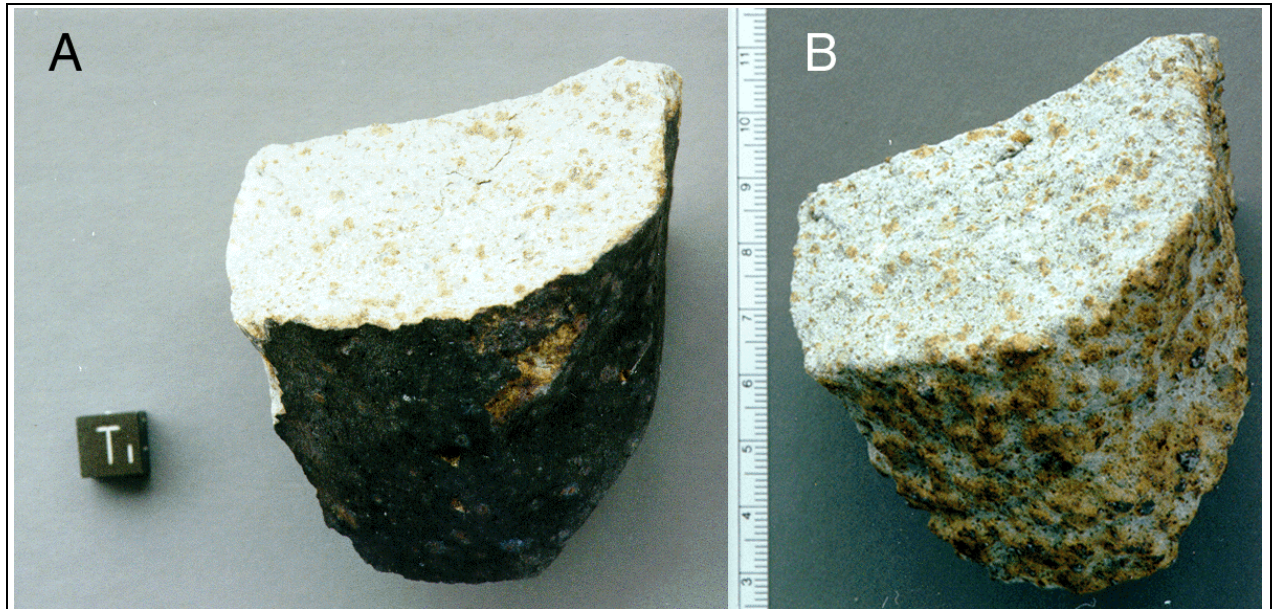


Figure 1. (A) The fragment of ALHA 85017 used in this study as it was received from the Meteorite Curator. The dark material is fusion crust; the darker spots on the fracture surface at the top are metal grains surrounded by oxidation halos. The cube is one centimeter on a side. (B) The fragment after it was sandblasted to remove the fusion crust. Note the concentration of oxidation on the surface that held the fusion crust. The major tick marks on the ruler are one centimeter apart.

some were always present. There is no evidence to suggest that this oxidation changed the macroscopic, structural strength of the sample.

The fragment was roughly equidimensional (Fig. 2), with a long axis of about 11 cm and a shortest near 6.5 cm. While the density of this meteorite was not measured, six L6 chondrites measured by Consolmagno and Britt (1998) present an average bulk density of $3.22 \pm 0.15 \text{ g cm}^{-3}$; five L6 chondrites measured by Yamogida and Matsui (1983) yielded an average of $3.30 \pm 0.07 \text{ g cm}^{-3}$. The former value is used in this paper for the density of 85017,13 because the samples measured by Consolmagno and Britt were larger than those in the latter study and are therefore probably more representative of bulk chondritic material. In any event, the difference between these two most likely values is just over 2% of their mean, so either could be used with little trepidation. Because the glass composing the fusion crust is not present in an asteroidal environment and would almost certainly interfere with some of the planned analyses, it was sandblasted from the meteorite with a pure SiO_2 sand.

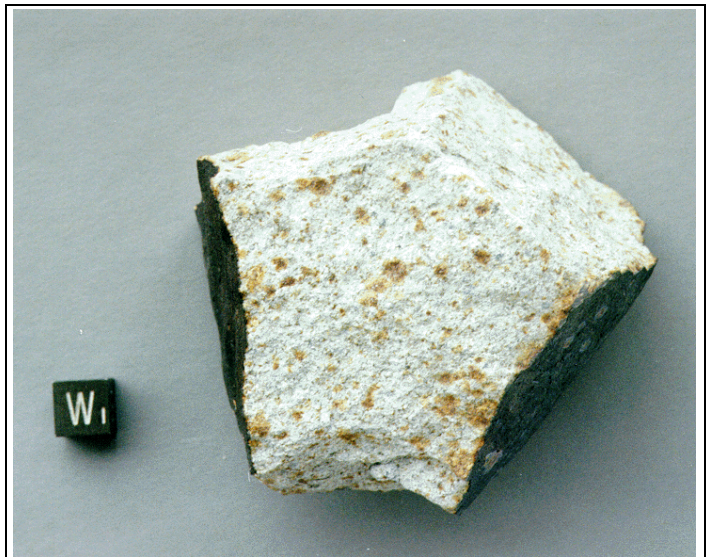


Figure 2. Another view of the meteorite fragment before sandblasting. The fracture surface visible in Fig. 1A is to the upper right and the fusion crust to the lower right. The cube is one centimeter on a side.

A total of 38.4 g of surface material was removed in the process, giving a pre-experiment mass (M_0) of 464.1 g.

Experimental Conditions

All of the impact experiments were performed with the Vertical Impact Facility at the Johnson Space Center. This is a powder-propellant range, although compressed gas can also be used for low-velocity impacts. To minimize oxidation effects during the experiments, dry nitrogen was used to displace as much air as practical from the impact chamber. The chamber was evacuated to <1 torr, flooded with dry nitrogen to 60 torr, and re-evacuated to <1 torr for each shot. The target fragment was suspended with thin, nylon monofilament, which minimized the area in contact with the fragment, inside a lexan box, which minimized the amount of debris lost per shot. The walls of the box were not padded, as it has been our experience that fragments thus prevented from breaking on contact with the walls of the container simply disaggregate anyway during sieving. After each shot, the largest remaining fragment was hung as the target for the next experiment; the impact vector passed near the center of mass of the target, but no two impacts occurred at the same point. The ejected and spalled materials were collected, sieved, and weighed. Fragments of the impactor were included in the sieved masses. Impacts continued until the mass of the largest remaining fragment (M_R) was less than $0.1 M_0$. This criterion was chosen arbitrarily to ensure that the target would be pulverized sufficiently for the ensuing regolith-evolution phase of the study (to be described in a subsequent paper); at the same time, it would provide additional disruption data (past the traditional 50% disruption point) for analysis.

Because the debris from the experiments would be analyzed with a variety of techniques including Mössbauer and reflectance spectroscopy, magnetically and optically neutral Al_2O_3 ceramic projectiles were used. Each was a sphere, 3.18-mm in diameter, with a mass of 0.065 g. The nominal impact speed was 2 km s^{-1} , and the actual average for these nine shots was $2.03 \pm 0.06 \text{ km s}^{-1}$, with a low value of 1.90 and a high of 2.12 km s^{-1} . These velocities yielded one-dimensional shock stresses between 17.7 and 20.5 GPa (177 and 205 kb) for this projectile-target combination, assuming impacts normal to the target surface and that the chondrite behaves as a dense basalt under these conditions (Appendix A, Table A1). Small-scale surface irregularities on the meteorite fragment (*i.e.*, on the order of the projectile diameter) made determination of the angle of impact impractical, but they were not necessarily normal to the local surface.

All implements used in the grain-size analysis were likewise metal-free. Sieves used for the bulk of the grain-size analyses were constructed from PVC cylinders and plastic mesh, while tweezers and sieve-cleaning tools were made from plastic and hardwood.

The Data

Dynamic data for the nine-shot series are presented in Table 1, and comminuted masses are listed in Table 2. (Note that, because the meshes were plastic, the smallest of the sieve openings used for these experiments was 120 μm . The distribution below this size was estimated by sieving an aliquant of the

Table 1. Dynamic data for the nine-shot collisional-disruption series. The density of the ceramic projectiles was 3.82 g cm^{-3} , while that for the chondrite was taken to be 3.22 g cm^{-3} . All experiments were performed at approximately 298 K. Shock stresses were calculated for normal impact, using a one-dimensional approximation. (See Appendix A.) The largest fragment remaining after shot 9 had a mass of 7.22 g.

Shot number	1	2	3	4	5	6	7	8	9
Impact speed (km s^{-1})	2.03	2.01	2.03	2.08	1.90	2.04	2.04	2.06	2.12
Initial target mass (g)	464.13	461.74	457.86	455.08	417.32	331.41	274.50	188.01	96.10
Shock stress (GPa)	19.3	19.1	19.3	20.0	17.7	19.5	19.4	19.7	20.5
Kinetic energy (ergs)	1.34×10^9	1.32×10^9	1.34×10^9	1.41×10^9	1.18×10^9	1.36×10^9	1.35×10^9	1.38×10^9	1.46×10^9
Momentum (g cm s^{-1})	1.32×10^4	1.31×10^4	1.32×10^4	1.36×10^4	1.24×10^4	1.33×10^4	1.33×10^4	1.34×10^4	1.38×10^4
Type of event	Cratering	Cratering	Cratering	Cratering	Partial disruption	Disruption	Disruption	Severe disruption	Catastrophic disruption

<120- μm fraction from shot 50 of the regolith series [Cintala et al. 2004]. This method was used in previous studies to compare the masses and surface areas of finer fractions of different experimental regoliths; in those cases, the <63- μm fraction was sieved. The rationale for this approach is explained in more detail in Appendix B.) In each of the first eight shots, the largest remaining fragment served as the

Table 2. Comminuted masses for each shot listed in Table 1. Masses are in grams. Values for grain sizes <0.12 mm were derived by sieving the <0.12 mm fraction after shot 50 of the regolith phase of the study. Please see the text for details.

Grain size (mm)	Shot Number								
	1	2	3	4	5	6	7	8	9
>16-32				26.94	58.46		44.16	52.26	
>8-16				4.83	9.03	36.99	17.32	19.60	63.46
>4-8	0.41	0.89	0.59	2.36	8.82	10.11	11.18	8.27	17.44
>2-4	0.75	1.23	0.38	1.37	4.08	4.95	6.51	5.09	7.72
>1-2	0.33	0.49	0.54	0.71	2.14	1.88	2.54	2.44	3.06
>0.5-1	0.14	0.26	0.23	0.32	0.97	0.84	1.23	1.06	1.26
>0.25-0.5	0.13	0.23	0.20	0.26	0.69	0.51	0.96	0.82	0.89
>0.12-0.25	0.12	0.19	0.18	0.21	0.53	0.47	0.76	0.63	0.66
>0.063-0.12	0.04	0.03	0.05	0.06	0.16	0.14	0.24	0.21	0.19
<0.063	0.16	0.14	0.23	0.28	0.67	0.58	1.00	0.89	0.80

target for the next experiment. Only the comminuted material was used for the sieve analyses when the largest remaining fragment was more than half the mass of the target as measured before impact. When no fragment was larger than half the target mass before impact (shot 9), all of the debris was treated as comminuted mass and was sieved.

Remaining Mass vs. Specific Impact Energy

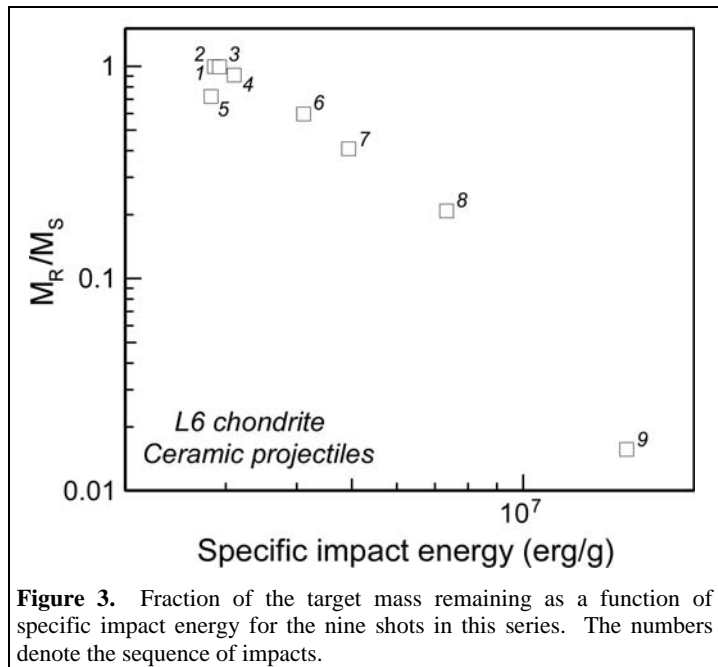
A standard means of illustrating the results of collisional-disruption experiments is used to display these data in Fig. 3, but in this case the mass of the target is the mass of the largest chondritic fragment remaining from the previous shot. As an example, the largest piece remaining after shot 3 had a mass of just over 457 g, which was impacted by shot 4; 457 g, therefore, was used to calculate the specific energy Q and the value of M_R/M_S (remaining target mass/pre-shot target mass) for shot 4. Fig. 3 displays a trend in M_R/M_S that is visually characteristic of a series of single-impact experiments.

The first three shots were essentially simple cratering events, a fact reflected in the minor change in target mass after each of those impacts. Large fragments began to spall from the meteorite with shot 4, whose data point in Fig. 3 shows the first notable loss of target mass. The specific impact energy was smaller for shot 5 because of the low impact speed, but it still removed an even greater fraction of the target's mass than shot 4, the second most energetic of the series. The specific impact energy grew rapidly with shots 6 through 9 because the target's mass decreased rapidly with each shot while the nominal impact speed (and absolute impactor energy) remained constant.

It is tempting to derive a value from Fig. 3 for Q^* , the specific energy at which nominal disruption occurs (*i.e.*, at which the largest remaining fragment is equal to half the original target's mass). Because the plotted values were derived from multiple impacts as opposed to the single-event disruptions normally used in such determinations, however, it would be potentially misleading to do so. Not only did the impact geometry vary throughout the series, but it is possible that the chondrite's strength degraded during the accumulating impacts. As a consequence, the best estimate of Q^* for ordinary chondrites as of this writing continues to be that determined by Flynn and Durda (2004).

Mass Distributions

The size distributions of the impact-generated fragments also show changes in form as the effects of the impacts evolved from cratering to fragmentation. This is apparent in Figs. 4a and b, in which the



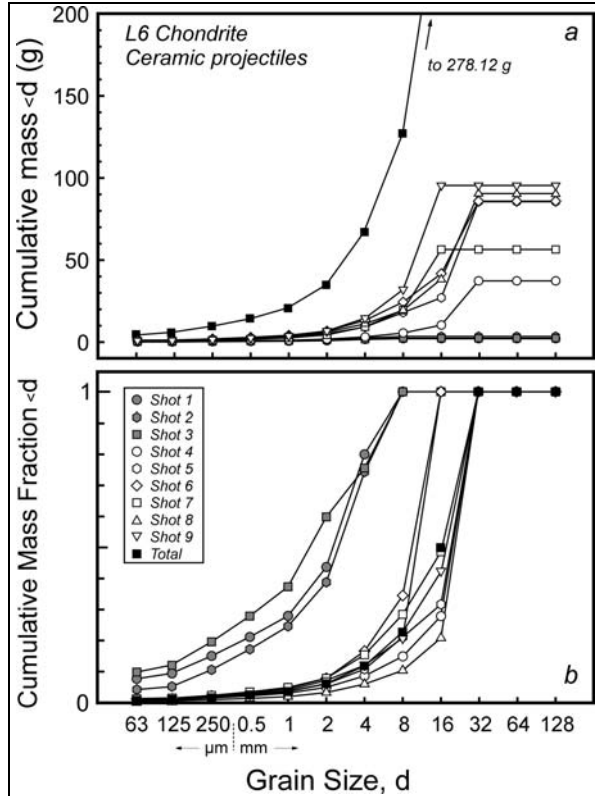


Figure 4. Size distributions of the fragments created during the 9-shot series. (a) Cumulative mass as a function of particle dimension for each shot. These are absolute quantities. Note the difference in curve shape and other characteristics between the simple cratering impacts (shots 1 through 3) and those resulting in some target disruption (shots 6 through 9). (b) Cumulative mass fraction of material displaced by each shot as a function of particle size.

disruptive events. When the largest one or two size fractions for each experiment are ignored, however, all of the distributions are remarkably similar in shape. Particularly interesting is the consistent, notable drop in mass from the 120-250 μm bin to the 63-120 μm bin and the corresponding enhancement of fragments <63 μm in dimension.

Surface Areas

It has been shown that well-defined relationships exist between impact energy and derived values of the newly created surface area (Cintala and

size distributions of the first three (cratering) shots present basically the same overall form. (Note that the largest remaining fragment is included in this figure only for the final shot of the series.) The trend from shot 4 is transitional between the form characteristic of crater ejecta from a solid-rock target and the pattern typical of disruptive events, in which larger fragments are spalled from the target mass. The randomness of that spallation process leads to the dissimilar shapes of the distributions at the larger grain sizes in Fig. 4b. As might be expected in a comparison of cratering and disruptive impacts, mid-sized fragments (1 to 8 mm) also are more abundant in the latter (Fig. 4a).

More details of the structure of each size distribution can be seen in a log-log plot of the mass in each size bin vs. grain size (Fig. 5). Shot 4 was disruptive in that it dislodged some large fragments, but its size distribution is still grouped more with the first three (cratering) impacts than with the remaining

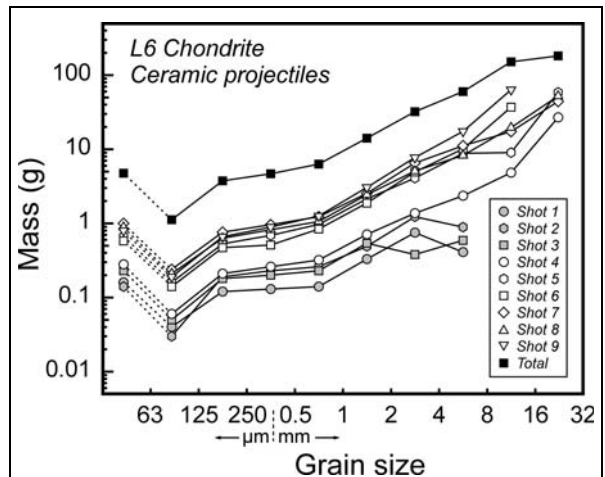


Figure 5. Mass of each sieved size fraction as a function of grain size. Values are plotted at the logarithmic midpoint of the bin limits. Dashed line segments represent the derived portion of the size distribution; see the text for details.

Hörz 1992), which is reasonable, since the energy expended in comminution is used to break inter- and intracrystalline bonds. Thus, the newly created surface area should be a better indicator of the comminution energetics of an impact than the comminuted mass: a single massive fragment can skew a mass distribution while representing a very small fraction of the new surface area and therefore of the energy partitioned into comminution (*e.g.*, Rubin et al. 1991).

The cumulative surface area created during the series is shown in Fig. 6 as a function of the impact energy accumulated by the remaining target. The surface areas were calculated with the cumulative size distributions shown in Fig. 4, assuming spherical fragments; please see Appendix B for details. (The same areas would result if cubes were assumed to represent the typical geometry instead of spheres; other geometries could be accommodated and would displace the points in Fig. 6 up or down slightly.) The trend is fairly well-defined and slightly concave upward for the first four shots in this log-log plot, after which the overall slope increases, implying that the last five shots were more effective in creating new surfaces. This is probably a consequence of at least three factors. First, the dimensions of the target decreased with each collision, placing its free surfaces closer to the impact point and making spallation more likely. Second, as the impacts accumulated, fracturing within the meteorite increased, weakening it. Subsequent projectiles thus found a target more susceptible to fragmentation. Third, the change from cratering to disruptive effects occurred between shots 4 and 5; beginning with shot 5, then, the total surface area represents the products of both cratering and disruptive components, the sum of

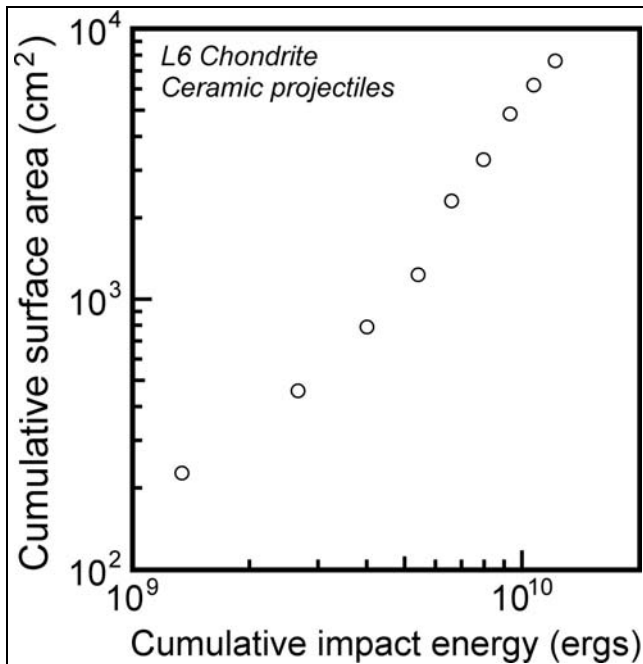


Figure 6. Derived surface area created throughout this series as a function of accumulated impact energy. Note the increase in slope after the fourth impact.

which obviously must be greater than that of the cratering component alone. Two steps in the trend occur: one between shots 4 and 5, and the other between shots 6 and 7, with the latter being considerably less dramatic. Again, the step between shots 4 and 5 could be attributed to the change in effects from cratering to disruption, but there could also be a component representing a change in fracturing efficiency due to some critical crack or flaw density being surpassed by shots 5 and 7 (Housen and Holsapple 1999).

Figure 6 can be compared to Fig. 7a to examine the effects of decreasing target mass as the series progressed. The overall shapes of both distributions are similar, but the curvature of the trend in the mass-normalized plot is more severe

than in Fig. 6. Indeed, the curvatures vary with the different segments and are probably caused by different phenomena. The path described by the lower four points is slightly concave upward, attributed here to the increased efficiency of surface formation due to internal damage in the target. In this view, the density of small fractures throughout the target increased as impacts accumulated, leading to a greater ease of comminution with time. This was diluted, however, by the erosion of target mass and the consequent drop in the value of M_s . Figure 7b illustrates the influence of this decrease by comparing the absolute cumulative energy with the mass-specific cumulative energy. The value of each data point can be viewed relative to the dashed line, which represents the relationship between the two values had the target mass been unchanged. Two principal factors, then, should contribute to the trend of Fig. 7a: internal damage, which facilitates comminution by weakening the

target, and the progressive reduction in target mass as material is spalled and ejected by the impacts. Thus, while the latter effect as illustrated in Fig. 7b is obvious in Fig. 7a, shock processing of the target is also important, as evidenced by the path described by the first four shots as well as by the jumps in surface area between shots 4 and 5 and between shots 6 and 7.

Comparison with Gabbro Targets

Many calculations in studies of asteroids and impact cratering often assume, for lack of other data, that chondritic bodies possess impact characteristics similar to those of terrestrial igneous rocks. In the interest of performing such a comparison, two additional impact series were conducted using pieces of Bushveldt gabbro as targets under conditions identical to those of the chondrite impacts. These were irregular chunks derived by mallet and chisel from a larger piece of gabbro, with dimensions roughly similar to those of the chondrite; their starting masses, 506 and 452 g, bracketed that of the chondrite

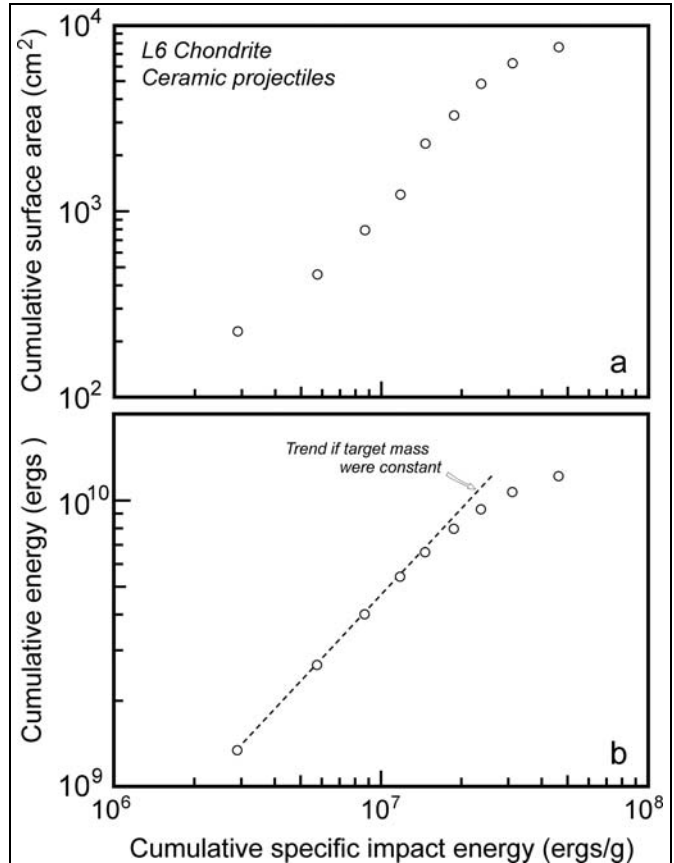


Figure 7. (a) Total surface area created as a function of the cumulative impact energy per unit target mass existing at the time of each impact. (b) Absolute cumulative impact energy plotted against its mass-relative counterpart. Note the nonlinearity introduced by the decreasing target mass as the number of impacts grew. The dashed line represents the curve that would have resulted had the target not lost mass because of the impacts.

target. Single-impact disruption experiments have demonstrated very clearly that considerable scatter characterizes many measures of the impact products (*e.g.*, Cerroni 1986; Housen and Holsapple 1990), much of which appears to be due to undetected flaws or weaknesses in the targets themselves (Rubin et al. 1991). Because of the potential for such spurious results, two gabbro series were performed; only one series, of course, was possible with the chondrite. Dynamic data for the two gabbro series are listed in

Table 3. Dynamic data for the two collisional-disruption series using Bushveldt gabbro targets with a density of 2.82 g cm^{-3} . Impact conditions were identical to those in the chondrite experiments. Shock stresses were calculated for normal impact with a one-dimensional approximation.

	Series 1					Series 2				
Shot number	1	2	3	4	5	1	2	3	4	5
Impact speed (km s^{-1})	2.10	2.10	2.07	2.08	2.07	2.05	2.07	2.03	2.07	2.06
Initial target mass (g)	506.44	473.89	470.78	463.04	425.85	456.22	451.18	437.93	371.72	303.71
Shock stress (GPa)	21.97	21.97	21.54	21.66	21.60	21.37	21.54	21.07	21.64	21.46
Kinetic energy (ergs)	1.44×10^9	1.44×10^9	1.39×10^9	1.41×10^9	1.40×10^9	1.38×10^9	1.40×10^9	1.34×10^9	1.41×10^9	1.39×10^9
Momentum (g cm s^{-1})	1.37×10^4	1.37×10^4	1.35×10^4	1.35×10^4	1.35×10^4	1.34×10^4	1.35×10^4	1.32×10^4	1.36×10^4	1.35×10^4
Type of event	Cratering	Cratering	Cratering	Partial disruption	Catastrophic disruption	Cratering	Cratering	Partial disruption	Partial disruption	Catastrophic disruption

Table 3.

Remaining Mass vs. Specific Impact Energy

The disruption paths for the three targets are notably different, particularly since seven impacts were required to disrupt the chondrite beyond the $0.5 M_R/M_0$ limit, while each of the gabbro targets needed only five (Fig. 8). As is common in disruption experiments, the impacts with low specific energies tend to exhibit rather aimless patterns. Only when the targets lose enough mass and/or when they are sufficiently processed by the previous impacts do the results begin to follow a better-defined trend. Given this, it is appropriate to note that the target in the first gabbro series maintained most of its mass until the fifth impact, which disrupted it catastrophically (*i.e.*, with a resulting M_R/M_0 below 0.5).

Figure 8 is somewhat misleading in that it does not illustrate the actual differences in energy required to disrupt the individual targets. Figure 9 is a similar plot but, using the cumulative specific

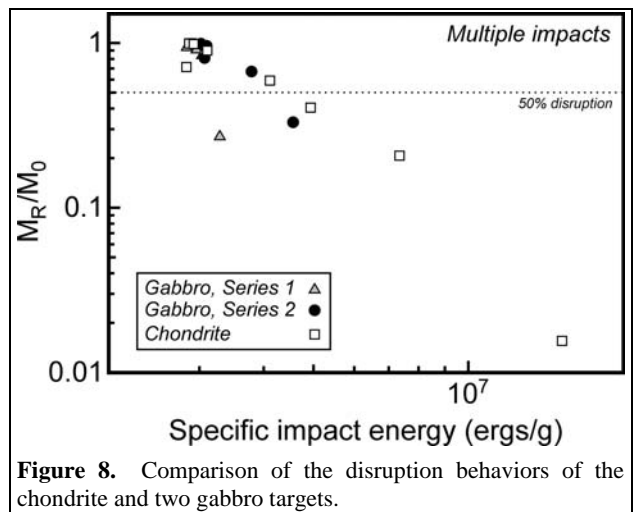


Figure 8. Comparison of the disruption behaviors of the chondrite and two gabbro targets.

impact energy instead, it is better at demonstrating the greater resistance of the chondrite to disruption under multiple-impact conditions. It is not clear if the cracks in the chondrite fragment noted before the

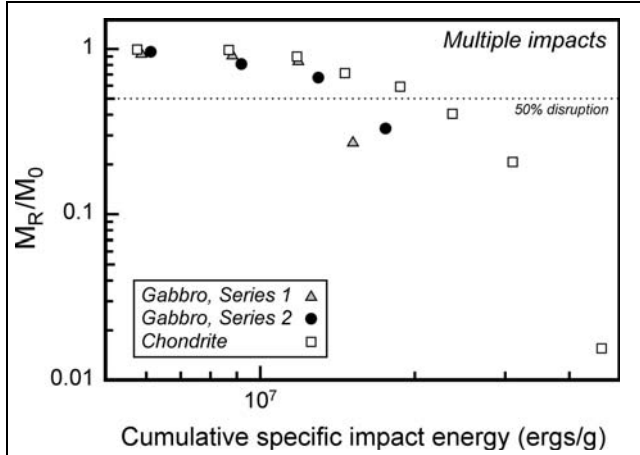


Figure 9. Disruption trends for the chondrite and gabbro targets as functions of the cumulative specific energy. This plot is a better illustration of the greater resistance of the chondrite to disruption.

accounting for the slight differences in point placement relative to some of the chondrite data in the 63-125- μm bin. The first gabbro target shed more large fragments throughout the series than the second, resulting in the more chaotic segments of the distributions at the larger grain sizes. The slopes of the gabbro distributions are somewhat shallower overall than those of the chondrite, but the chondrite distributions possess a more uniform structure. Perhaps most obvious are the chondrite's relative lack of debris in the 63-120 μm bin and its abundance of <63 μm fines. These features are illustrated more obviously in Fig. 11, which presents the data from Fig. 10 normalized to the chondrite distributions.

Surface Areas

If the surface area generated by an impact could be used as a measure of the energy partitioned into comminution, then Fig. 12 would be an illustration of that energy sink's variability. Specifically, the surface areas created in both gabbro series were consistently greater than those of the chondrite until the disruptive effects began in the latter after shot 4, following which

experiments began had any effect on the target's behavior during impact; if anything, they should have weakened it. Thus, the fragmentation trend observed in Fig. 9 must be considered as representing its minimum resistance to disruption.

Comminuted Masses

The nature of the comminuted debris for each gabbro series is depicted in Fig. 10, in which both targets are compared to the chondrite. Note that a standard (metal) sieve set was used to determine the gabbro's size distributions,

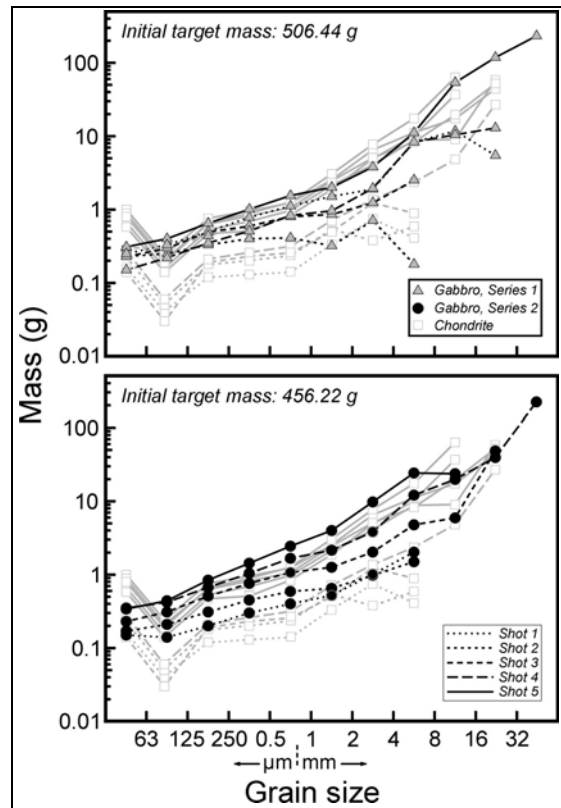


Figure 10. Comparison of the absolute mass distributions created in the two gabbro series with those generated in the chondrite experiments. Only the first four experiments of the chondrite series are specified by the different line types; the fifth shot in that series is the lower member of the distributions described by the solid gray lines. Data are plotted at the logarithmic midpoints of their respective size bins.

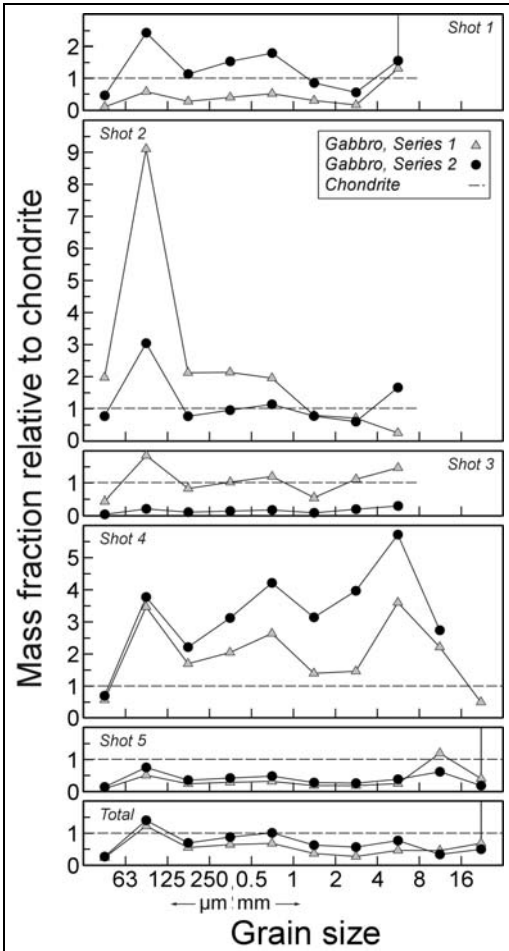


Figure 11. Comparison of the size distributions of the debris from the chondrite and gabbro experiments. The value for each size bin was first calculated as the fraction relative to the entire mass comminuted in that particular experiment; it was then divided by the relative mass fraction of chondritic material in that size fraction. (The 63-125- μm gabbro fractions were divided by the 63-120- μm chondrite fraction.) Thus, the debris from the chondrite experiments plot as the straight line with a constant value of 1. As each gabbro series comprised only five shots, the final four chondrite experiments are not presented here. Vertical line segments result from no chondritic mass being present in that size bin.

was not pristine, the results presented in this contribution must be considered accordingly. Specifically, an unaltered, unfractured, L6 chondrite that did not survive passage through a planet's atmosphere and impact on its surface might well be more coherent and could require more kinetic energy partitioned into comminution to attain a given degree of disruption than these experiments might suggest. Thus, these results should be treated as describing the behavior of pristine L6-chondritic material at a lower limit of resistance to disruption, which could be an academic point, as the last pristine undifferentiated meteoritic

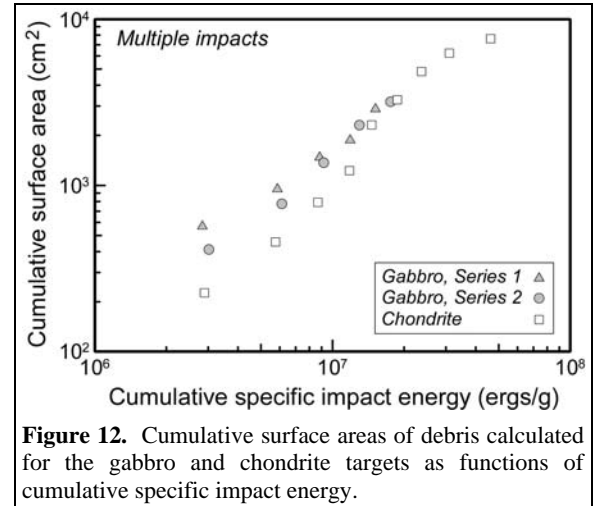


Figure 12. Cumulative surface areas of debris calculated for the gabbro and chondrite targets as functions of cumulative specific impact energy.

essentially no difference between the chondrite and either of the two gabbro series was noted. The slopes from both gabbro series were lower than that from the chondrite shots, and the first set of gabbro results hints of a jump in comminution efficiency reminiscent of that between shots 4 and 5 in the chondrite series. The evolution of surface areas in the second gabbro series falls between those of the first gabbro set and the chondrite. As with the chondrite, the gabbro trends before disruption are concave upward, indicating that comminution became easier with accumulating impacts.

Discussion

General disruption and comminution mechanics — As described earlier, the chondritic fragment used in this series of experiments exhibited macroscopic evidence of both oxidation and pre-existing fracturing. Because this sample

material probably became extinct during or soon after the formation of the solar system. Nevertheless, this chondrite presented itself as a stronger target to the impactors than did the gabbro.

Dolomite and basalt targets were also impacted with the intention that they too would serve as comparisons for the chondrite, but the dolomite fractured along bedding planes and the basalt along preexisting fractures, giving misleadingly low values for the energy necessary to meet the criterion of

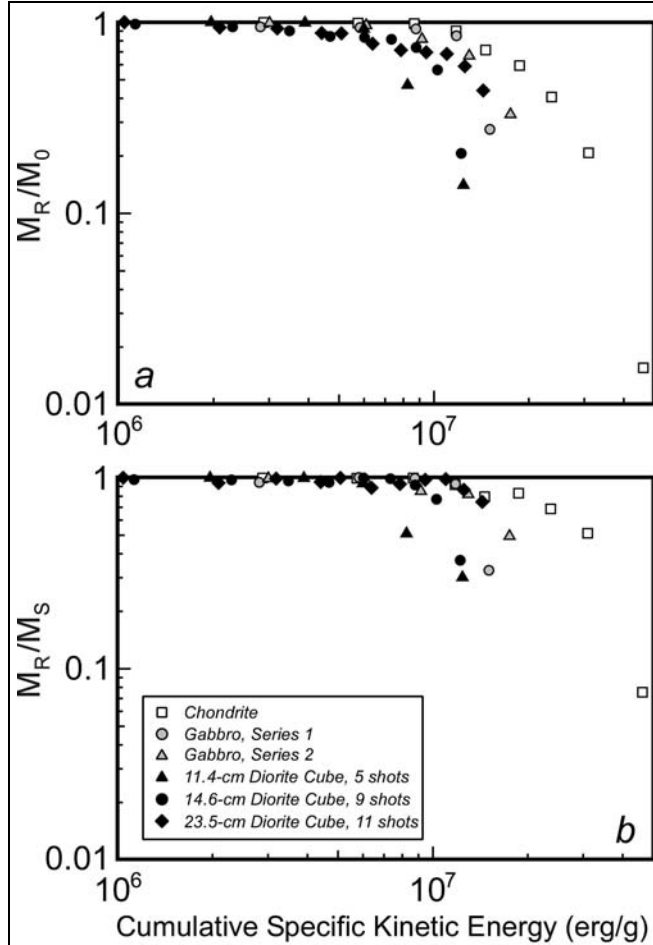


Figure 13. Comparison of the multiple-impact disruption trends for the irregular chondrite and gabbro fragments and diorite cubes. (a) The largest remaining fragment presented as a fraction of the mass of the initial target before it was subjected to the first impact (M_0). (b) The largest remaining fragment as a fraction of the target mass presented to each shot in the series (M_s). The greater resistance of the chondrite to disruption is apparent in both versions.

50% disruption. They are therefore not included in this discussion. An earlier series of multiple-impact experiments (Hörz et al. 1985), however, used sawed and thus unfractured cubes of "Sierra Gray" granodiorite as targets, and those results can be used here for additional comparisons with the chondrite (Fig. 13). The cubes were impacted by stainless-steel spheres either 6.35 or 12.7 mm in diameter, depending on the series; nominal impacts into the granodiorite were at 1.0 and 1.4 km s⁻¹, again depending on the series. Impacts were initially normal to the target's surfaces, but as mass was removed and the targets became more irregular, random incidence angles were the rule. No allowance was made for the differences in impactor material or impactor size in generating Fig. 13, but previous experiments demonstrate that the degree of target fragmentation as a function of specific impact energy at these velocities is independent of impactor material, at least to within the scatter in the data (*e.g.*, Cintala and Hörz 1984). Indeed, it appears that undetected variations in the condition of the

target material are more important in determining the degree of fragmentation (Rubin et al. 1991). Housen and Holsapple (1999) have demonstrated that the absolute size of the target plays a major role in its relative strength, but the range of sizes treated here is too restricted to expect manifestation of such an effect. While there appear to be indications of a trend as a function of size for the diorite targets in Fig. 13, it should be noted that the largest targets were impacted by 12.7-mm spheres while the two smaller

targets sustained impacts from 6.35-mm projectiles. In any case, the maximum dimension of the chondrite used in this study was essentially equivalent to a side of the smallest diorite cube included in Fig. 13; if size were a dominant factor in establishing whatever hierarchy might be interpreted to exist in the figure, then the chondrite and smallest diorite targets should have produced similar trends.

Given all of these considerations, the greater resistance of the chondrite to disruption is remarkable, particularly since cracks were visible on the surface of the meteorite fragment and some metal grains in its interior were obviously oxidized. The behaviors of the gabbro and granodiorite targets were more similar to each other than to the chondrite, with both clearly being less resistant to disruption. The reason for the toughness of the chondrite under these impact conditions is far from certain, but an additional set of observations could provide insight into the unusual behavior of the chondrite.

Fig. 14 presents the size distributions of debris from each of the series included in Fig. 13; to put the different series on a more even footing for comparison, the values used in Fig. 14 are those following the impact in each series when M_R/M_0 became less than 0.5. The figure demonstrates that a notably greater relative fraction of fine (<120 μm) material was derived from the chondrite than from the gabbro or granodiorite. Even allowing

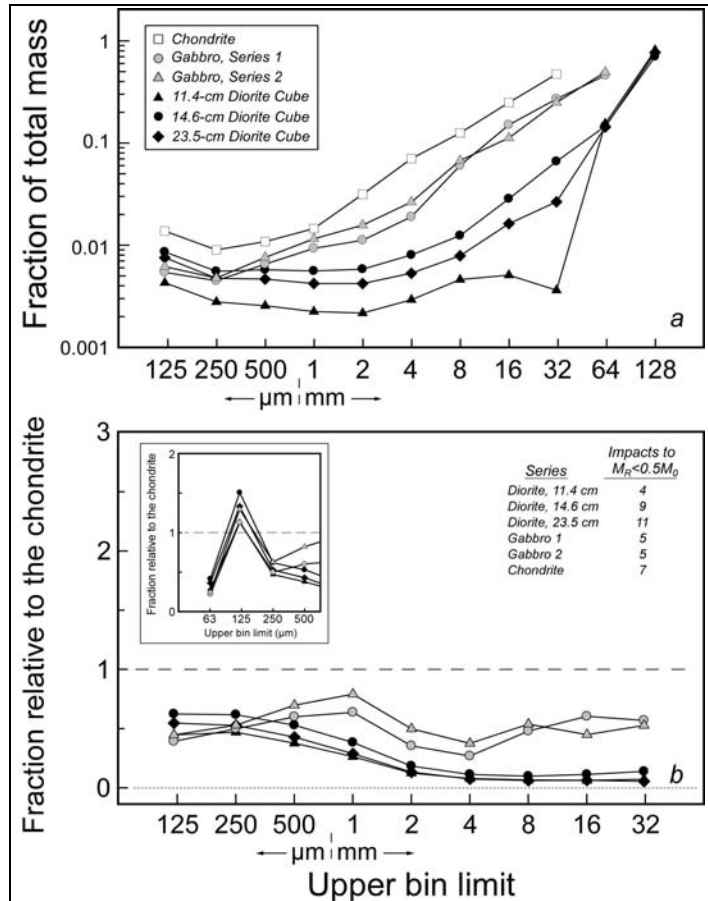


Figure 14. Comparison of grain-size distributions for the chondrite, gabbro, and three granodiorite targets subjected to multiple impacts. Each set of points represents the size distribution following the impact at which the mass of the largest remaining fragment became less than 50% that of the initial target. The number of impacts required to reach that point for each series is tabulated in (b). (a) Size distributions for the six targets presented as fractions of the total displaced target mass. Note that the chondrite provided substantially more material finer than 120 μm than did either of the other two target types. (b) The same data as in (a), but presented relative to the mass of chondritic material in each size bin. (Inset) The same data as in (b), but with the finest fraction sieved to 63 μm , emphasizing the relatively small amount of chondritic material in the 63-120 μm fraction. The enhancement of debris smaller than 63 μm more than makes up for the shortcoming in the chondritic 63-120 μm fraction. Note that the material in the >32 mm size fractions from the diorite experiments are not included in (b) because their abundance relative to the chondrite, with no fragments larger than 32 mm, would be infinite.

for the 63-125 μm enhancement of the gabbro and granodiorite over the 63-120- μm chondrite fraction, the chondrite produced an average of twice as much material smaller than 120 μm (Fig. 14b). Thus, as

Fig. 13 shows, the chondrite was more resistant to disruption in general than either the gabbro or the diorite, yet it yielded greater relative fractions of fines than the other two rocks (Fig. 14). This behavior is similar to that found in the laboratory for "regoliths" of monomineralic olivine (Cintala and Hörz 1992).

Figure 15 shows a view of one of the coarsest parts of this meteorite as observed in thin section. ALH 85017,13 is a compact rock; a survey of three thin sections (ALH 85017,22; ,32; and ,24) showed no evidence of porosity other than fracturing, typical examples of which are displayed in this view. The scale bars demonstrate that the majority of the meteorite's texture is on a scale below 120 μm ; even those crystals with dimensions above 120 μm are heavily fractured. A spate of recent studies of ordinary-chondrite density and porosity (*e.g.*, Britt and Consolmagno, 2003; Consolmagno and Britt, 1998; Consolmagno et al., 1998; Flynn et al., 1999; Wilkison et al., 2003; Wilkison and Robinson, 2000) have shown that L chondrites possess a range of porosities with an average near 10%. L6 chondrites appear to

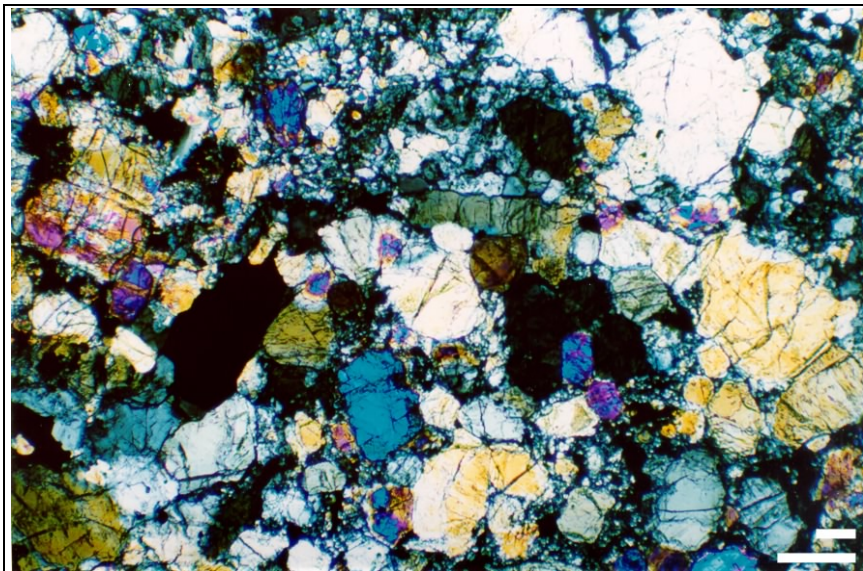


Figure 15. Photomicrograph of a coarser-grained section of ALH 85017,13. Note the fine-grained groundmass and the pervasive fracturing of the larger crystals and clasts. The top and bottom scale bars in the lower right are 63 and 120 μm long, respectively. A smaller version of this figure appears as the small frame in Fig. 16.

average closer to 6%, with a range around that value assumed by Britt and Consolmagno (2003) to be due to differing degrees of cracking in the individual samples. Because there is no evidence in thin section for any other form of porosity in ALH 85017, it is also assumed here that whatever porosity this sample might possess must be manifested in the observed fracturing. Thus, while L6 chondrites are

among the most highly metamorphosed and annealed undifferentiated meteorites, this individual has undergone fracturing after the annealing event at least on the scale of its coarsest mineral constituents. Given the scale and extent of the fracturing apparent in Fig. 15, then, it is reasonable to assume that any stress wave able to liberate one of the large crystals from its matrix would also disaggregate the crystal itself.

The gabbro and granodiorite are pristine rocks compared to the chondrite in terms of the density of preexisting fractures, (Fig. 16). Thus, the large enhancement in the fines produced during the chondrite experiments could be indicative of reactivation of those fine-scale cracks observed optically. A candidate hypothesis can be described as follows. The chondrite is a highly annealed and indurated rock but, because of its texture, it is difficult to propagate cracks leading to wholesale fracturing and spallation. Once a level of stress exceeding that of crack reactivation is reached, crack propagation is diffused because of the many available fracture pathways. (This is perhaps analogous to the relative-strength analogy for rubble-pile asteroids, in that their fragmental nature and porosity could attenuate stresses very effectively, localizing shock effects to a region around a given impact site [Asphaug et al. 1998].) When the stress wave is strong enough to rupture the rock, the fracture zone, measured on the scale of the thickness of the stress pulse and hence comparable to the dimensions of the impactor, encompasses a volume of grains bounded by preexisting cracks. Thus, when the chondrite failed under these impacts, it did so predominantly through crack reactivation and consequent generation of large quantities of fines. Even in the early shots of the series, best characterized as cratering events, more fines typically were created from the chondrite than from the gabbro, reinforcing this view.

The gabbro, on the other hand, is holocrystalline, with the dimensions of most of its component grains in the range of 2-4 mm. Thus, it is the opposite end-member here in terms of crystal size. ("Crystal" here refers to a constituent mineral grain of the rock, so called to avoid confusion with the "grain size" used to describe the sieved products.) This gabbro tended to fracture along grain boundaries in previous regolith-evolution

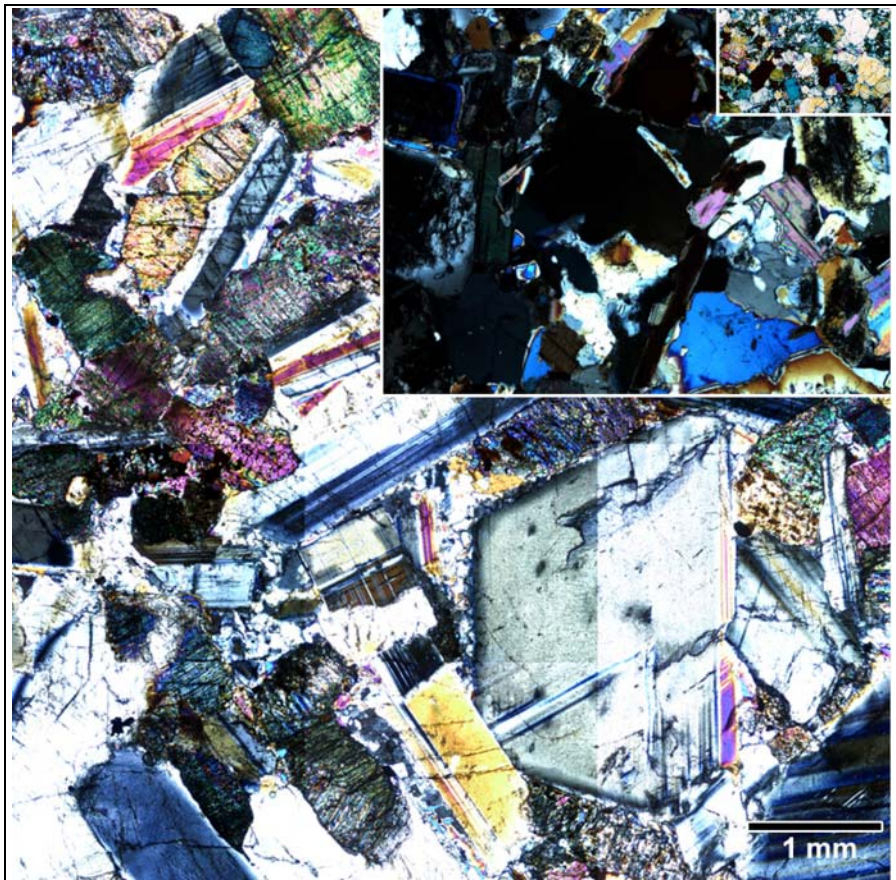


Figure 16. Cross-polarized thin sections of the Bushveldt gabbro (largest frame), the granodiorite (mid-sized frame), and the chondrite ALH 85017 (smallest frame, upper right), all to the same scale.

experiments (Hörz et al. 1984), enhancing the mass in the 2-4-mm size bin over those of the adjacent size fractions as soon as the first impact in those series (Cintala and Hörz 1988). There does not, however, appear to be an equivalent mass enhancement in that size range in the gabbro experiments shown in Figs. 10, 11, or 14. While this could be due to the difference in target configurations between these (single, massive fragments) and the earlier experiments (multiple, 16-32-mm pieces), even the first shot in each of the regolith experiments showed mass enhancement in the 2-4-mm fraction (Hörz et al. 1984; Cintala and Hörz 1988). Given the masses of comminuted debris created by the initial shots of the regolith experiments, it is likely that most of the comminution products came from one to perhaps three fragments, so at least the first shot in each of those series can be treated as a small-scale disruption experiment at high specific energies. Because mass excesses in the 2-4-mm fraction were observed in experiments using stainless-steel impactors at three different impact speeds (0.7, 1.4, and 1.9 km s⁻¹; Cintala and Hörz 1988), impact speed (or magnitude of shock stress) alone can be ruled out as the main factor for this enhancement.

The principal remaining difference between the gabbro regolith and disruption experiments was in the projectiles; the regolith experiments used 6.35-mm stainless-steel spheres, while the ceramic impactors used in this study were half that size. Two possibilities exist: the difference in density or strength between the two impactor materials could have contributed, and/or impactor size could be a factor. The behavior of the stainless-steel spheres is instructive in this regard (Cintala and Hörz 1988). The 0.7-km s⁻¹ spheres maintained their integrity with only incipient fracturing occasionally being visible. The 1.4-km s⁻¹ impactors were broken into a few large pieces, but most of the disrupted 1.9-km s⁻¹ projectiles could be removed from the target only magnetically as fine-grained debris. Thus, projectile-target coupling covered the range from simple collision and rebound of the projectile to mutual pulverization. The fate of the ceramic impactors at 2 km s⁻¹ was similar to that of the high-speed stainless steel, in that both were pulverized. For this reason, it is doubtful that the mode of transfer of impactor energy or momentum differed for the two projectile materials.

The density contrast between the impactor and target manifests itself in the magnitude of the shock stress. The highest shock stresses possible in the 1.9 km s⁻¹ regolith experiments were 22 GPa (Cintala and Hörz, 1988), which is effectively identical to those calculated for the two disruption series discussed here (Table 3). The differences in the comminution behavior therefore do not seem to be due to impactor density or strength.

Thus, it appears that the comminution behavior of the gabbro was influenced by the impactor size, probably through the length or duration of the shock pulse. Effects due to the relative thickness of the shock pulse have been suggested before in the context of asteroid disruption (*e.g.*, Martelli et al. 1994; Asphaug et al. 1998) and penetration of thin targets (Hörz et al. 1995); they have also been the subject of

more recent experiments and numerical studies (Barnouin-Jha et al. 2002). A simple, one-dimensional evaluation of the geometry of the stress pulse can be instructive; to this end, a simple equation for the thickness λ of a one-dimensional shock pulse is derived in Appendix A and found to be

$$\lambda = \frac{l_0}{U_p^2} (U_t - u_t) (2U_p - u_p) \quad (\text{A10})$$

in which U_t and u_t are the shock speed and particle speed behind the shock in the target, respectively, U_p

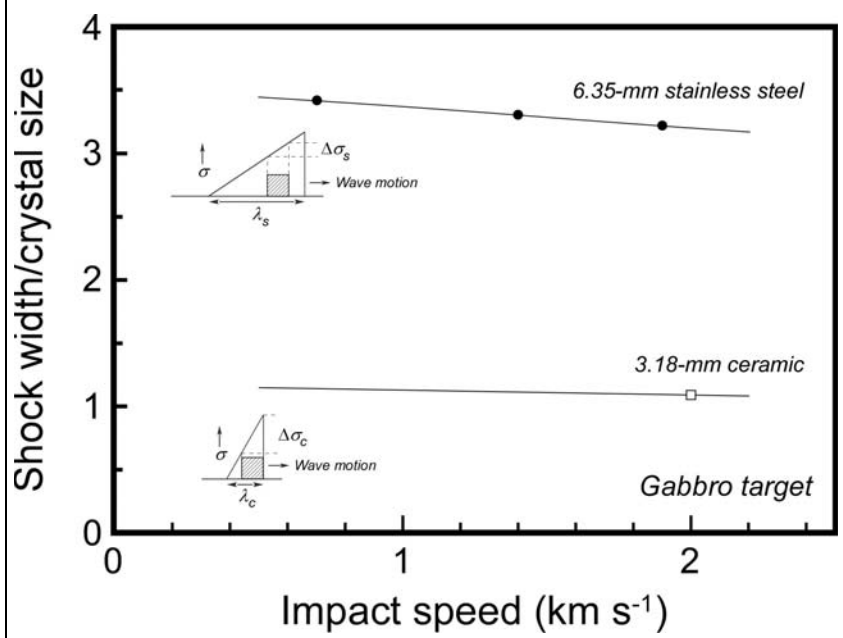


Figure 17. Calculation of the approximate width of a one-dimensional shock pulse relative to the mean dimension of crystals composing the gabbro for stainless-steel and ceramic impactors. Each impactor type is represented by its own curve; the points indicate the nominal impact speeds used in the two sets of experiments. Below each curve is a simplified schematic diagram of the relationship between the length of a stress wave and the stress difference $\Delta\sigma_x$ across an idealized grain (hatched square). The stress waves will be proportional to the shock thicknesses and are represented here as right triangles. (Note that in the one-dimensional approximation without losses to entropy, they would be rectangular.) The two waves depicted here have identical amplitudes. Note that the shorter the wavelength of the stress wave (in this case, λ_c), the greater the net stress difference across the grain because of the steeper stress gradient. Any reflection of such a wave back through the crystal will intensify that stress difference.

is the shock speed in the impactor, and l_0 is the length of the impactor. When a shock penetrates into the target in a three-dimensional situation, it will drop in intensity, smearing out, attenuating, and losing its identity as it encounters grains of different shock impedance and physical condition, and as rarefactions consume the shock when it encounters free surfaces. Nevertheless, (A10) can be used as an approximate value that is well-defined and useful for comparative purposes.

The sizes of the two different impactors used in the gabbro experiments can be accommodated by calculating

the ratio θ_s of λ to the size of the average crystal κ composing the gabbro (~ 3 mm), viz.,

$$\theta_s = \frac{\lambda}{\kappa} = \frac{l_0}{\kappa U_p^2} (U_t - u_t) (2U_p - u_p) \quad (1)$$

Values for θ_s are plotted in Fig. 17 for the gabbro over the speed range of 0.5 to 2.2 km s⁻¹ for the 6.35-mm stainless-steel and 3.18-mm ceramic impactors. In both cases, the shock thickness is only weakly dependent on the impact speed over the range used in the experiments. The shock thickness from the larger impactors, however, is much greater than the mean crystal size across the range of speeds, and indeed all analyzed impacts by the stainless-steel spheres resulted in mass enhancement of the 2-4-mm fraction. Impacts by the smaller ceramic spheres, however, produced a shock thickness that was a fraction of those in the stainless-steel experiments and closer to the mean crystal dimension. A description of the highly complex phenomenological relationship between the thickness of the shock and the detailed comminution of a given polycrystalline target is beyond the intent of this paper but, given the combination of the earlier gabbro results, the experiments described here, and Fig. 17, it is clear that the thickness of the shock could be important in determining the characteristics of the comminution products. There are two ways that the shock thickness relative to the crystal size could manifest itself in the way that the target is comminuted: the duration of the shocked state and the stress gradient. In the context of brittle fracture such as that discussed here, it seems that the only means by which shock duration could be related to the style of comminution would be through some characteristic activation time. For instance, in order to disrupt a grain, the time taken to activate a fracture would have to be shorter than the duration of the stressed state. Because the decompression period typically would be comparable to that of compression (*e.g.*, Melosh, 1984), this time could be considered as being roughly equal for both types of failure. Fine-grained material was generated from all of the gabbro targets, however, so any such activation time that might govern the fracture of constituent crystals was exceeded in all cases. Thus, stress duration is not the explanation for the different gabbro results.

The stress gradient is related to the shape of the wave, its length, and its peak amplitude (*e.g.*, Rinehart, 1975; Melosh, 1984). The two small illustrations in Fig. 17 near stainless-steel and ceramic curves are highly idealized, schematic diagrams of stress vs. distance for stress waves generated by each impactor type. The peak stress is the same in both cases, but the stress decay for the larger stainless-steel projectile is slower than it is for the smaller ceramic impactor; these wavelengths and thus the stress gradients are related to the thickness of the shock. The hatched square represents a gabbro grain at the same scale in each case. Because of the shorter wavelength associated with the ceramic sphere (λ_c), the stress difference $\Delta\sigma_c$ across the characteristic dimension of the grain is greater than the equivalent stress difference $\Delta\sigma_s$ in the stainless-steel case. This drastic simplification for illustrative purposes does not include the effects of reflected waves, which can be numerous; the interaction between shear, compressional, and tensile waves; multiple grains; etc., but it serves to show how the shock thickness could play a very important role in the mode and scale of comminution in such impacts. For instance, if the waves depicted in the figure were tensile in nature, and if $\Delta\sigma_c$ were greater than the tensile strength of

the grain, the grain would disrupt. On the other hand, with $\Delta\sigma_s$ being less than the stress required for failure, the wave created by the stainless-steel impact would be more likely to leave the grain intact. Because the comminution process would consume significant amounts of energy contained in the shorter wave, its total energy and, therefore, its amplitude would decrease much more rapidly than that of the longer stainless-steel wave. This effect would account for the fact that the most thorough comminution occurs near the impact site. The longer wave, however, could more effectively exploit larger, weaker defects such as preexisting cracks or grain boundaries.

When compared to the relatively easily characterized gabbro, the chondrite represents a pathological case insofar as the variance in its crystal size is so great that a value for κ , even if it could be determined, would have little relevance for this purpose. If ALH 85017 could be disaggregated only by separating the grains and crystals without comminuting them, it is not obvious from thin sections that the resulting mass in any one size fraction would dominate the others. Because the impact process is not so selective, however, the meteorite favors more thorough comminution because of its fractured nature than does the more pristine gabbro. This, reinforced by the large portion of crystals and matrix smaller than $63\ \mu\text{m}$ in the chondrite, manifests itself in the mass enhancement in the chondritic debris at sizes below $63\ \mu\text{m}$.

Mass-number distributions — Other than the largest fragment of ejecta and the largest fragment remaining after each impact, no other individual masses from the meteorite were measured in order to avoid excessive and potentially disruptive handling of the debris. The overall trends for the number of fragments in a given mass range, however, can be extracted from the sieve data (Appendix B). The numbers derived from these data are dependent on the geometries of the modeled fragments, since each shape defines an individual fragment's mass and hence the number in a given sieve fraction. In the following discussion, "fragment size" and "fragment dimension," as plotted in the figures, refer to the size of the mesh through which a fragment passed.

As described in Appendix B, the size distribution in each sieve fraction is treated as being continuous between the dimensions defined by the sieve openings. Fragments were modeled with five different geometries: spheres with diameters equal to the fragment's dimension, cubes with sides equal to the fragment's dimension, 0.5:1:1 prisms with the larger sides equal to the fragment's dimension, 1:1:2 prisms with the smaller sides equal to the fragment's dimension, and 1:1:2 prolate spheroids with the smaller axes equal to the fragment's dimension. (As an example, the largest fragment in the 0.5-1-mm size fraction, when modeled as a cube, would have dimensions of $1\ \text{mm} \times 1\ \text{mm} \times 1\ \text{mm}$; when modeled as a 1:1:2 prism, it would have dimensions of $1\ \text{mm} \times 1\ \text{mm} \times 2\ \text{mm}$.) The greatest volume differences and hence the largest variation in the calculated number of fragments was between the 0.5:1:1 and 1:1:2 prisms. The numbers from these two geometries are then used to bracket the most likely values. Figure

18 illustrates the number of fragments larger than the fragment size for each of the nine impacts in this series. Shots 1 through 4 were cratering impacts, shot 5 was transitional between cratering and

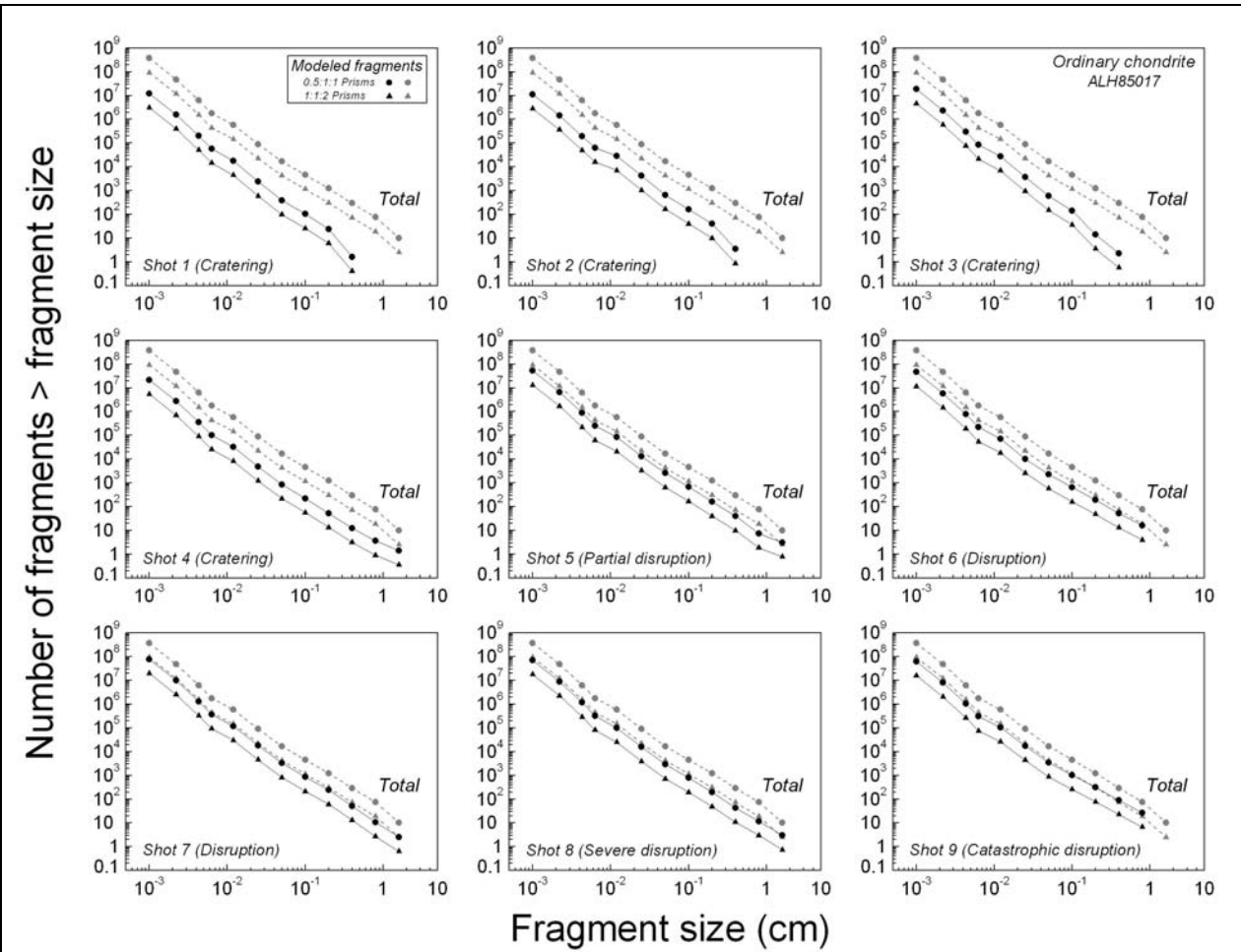


Figure 18. Number of fragments produced by each of the impacts compared to the total at the end of the series. The two prismatic geometries were used to calculate the values in this figure to bracket the most likely minimum and maximum numbers. The dashed, gray plots indicate the totals for each geometry at the end of the nine-shot series; they are included as referents in each of the panes to facilitate comparisons between the plots. Because the same size distribution was used to calculate the masses of debris in the fractions below 63 μm , the shapes of all of the distributions in this figure below 63 μm are the same. The obvious kink in all of the distributions near 63 μm is due to the relatively small amount of material in the 63-120 μm fraction.

disruption, and the rest were disruptive, with shots 8 and 9 being the most destructive. These differences are apparent in the figure: the cratering events, with higher overall shock stresses per unit of mobilized volume, yielded a greater fraction of small fragments than the disruptive impacts, and therefore display steeper overall slopes (Öpik 1971; Oberbeck 1975). The last shots of the series, which created large chunks of fragmented chondrite, are recognizable by the trends with lower slopes, particularly at the larger sizes.

More information can be derived from the chondrite's fragment-number distributions by comparing them to the data from the two gabbro series. This is done in Fig. 19, which displays panels for each of the five gabbro shots as well as a panel for the cumulative-number distribution of all debris

created in each series. Since the numbers for fragments modeled as cubes fall roughly midway between those for the two prismatic geometries used in Fig. 18, the cubic geometry is used in Fig. 19 as being representative, keeping the number of distributions in each panel to a minimum.

The first two impacts in each of the three series resulted in craters, although the second gabbro target lost more mass through spallation than did either of the other two targets; this is reflected in the "hump" at the larger-fragment end of the distribution. Otherwise, the slopes for all three series are

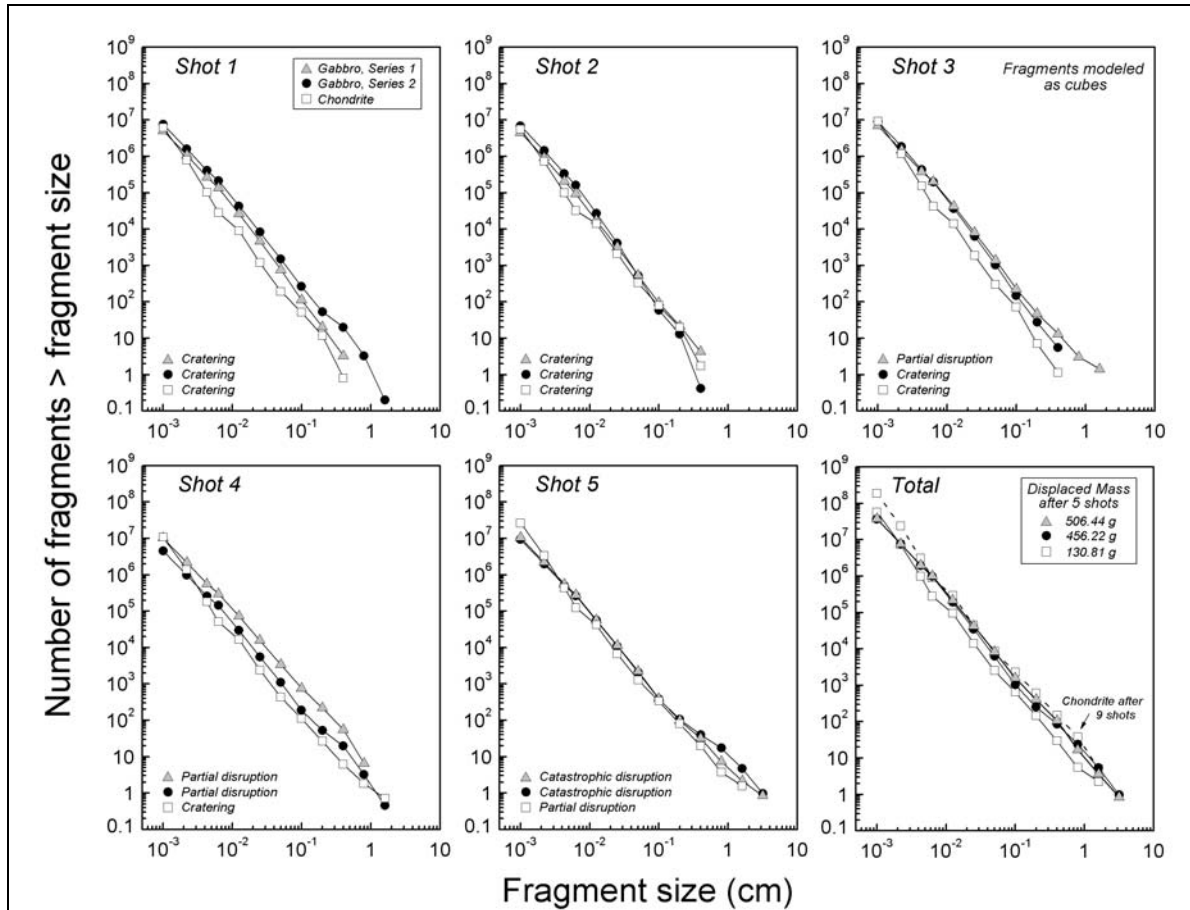


Figure 19. Cumulative number of modeled fragments from the chondrite and two gabbro series. All of the fragments in this figure were modeled as cubes, as that geometry gives results intermediate to the two different prism shapes used in Fig. 18. The distribution of all fragments at the end of the nine-shot chondrite series is included for comparison in the last pane (open squares and dashed line). The result of each shot is described in the lower left corner of the first five panes.

similar, although the chondrite shows the relative lack of material in the 63-120- μ m range even after the first shot. The third shot produced similar quantities and distributions of debris from both gabbro targets, which behaved similarly over most of their range; the larger fragments from the partial disruption in the second series shaped the distribution at its larger end. The chondrite's trend is mostly unchanged from the first two impacts in both position relative to those of the two gabbro experiments and in shape; since all three chondrite impacts were cratering events, this is not surprising. The fourth impact resulted in partial disruption of both gabbro targets. While the fourth impact into the chondrite was still in the cratering

regime, it was closer than the previous three to being a disruption event, a fact reflected in the greater fraction of coarser debris. Shot five resulted in catastrophic disruption of both gabbro targets and the first partial disruption of the chondrite. All three distributions are remarkably similar except at the very largest sizes, where the gabbroic debris dominates, and at the smallest sizes, where the chondritic debris is distinctly more abundant.

When compared, the distributions of all the debris after the five impacts are revealing. Assuming that the derived fragment numbers follow Poisson distributions, the two gabbro samples can easily be described by a single trend within the uncertainties, except for shot 4. (Error bars are not plotted in the figure for the sake of clarity.) Most of the chondrite's mass after the fifth impact still resided in a single piece, so most of the debris was contained in finer fragments, giving a slightly steeper slope and a smaller overall number of fragments. When the chondrite's results after the ninth impact are compared, however, the only notable difference with the two gabbro series is again in the finer fractions. In terms of fragment numbers, then, the following can be concluded: because it presented a weaker target, the gabbro evolved larger fragments earlier in the series of impacts than the chondrite did. The gabbro also yielded the largest fragments overall. By the time total disruption occurred, the fragment-size distributions of both gabbro targets were almost indistinguishable from the chondrite's except for a few larger fragments produced from the gabbro and a substantially greater number of fines from the chondrite. Since fines characteristically require greater expenditures of energy to produce than larger fragments, the creation of more fines is consistent with the chondrite being a stronger target than the gabbro. This is supported by the fact that catastrophic disruption of the chondrite required about 80% more energy than did the gabbro targets.

Fragment numbers as a function of size from disruption experiments are available in the published literature. Those data, however, often occur at a higher resolution in terms of numbers than do those calculated here for the chondrite, because individual fragments in the former are often counted and their masses measured. On the other hand, much smaller fragments can be included here, because their numbers do not rely on individual counts but instead are calculated from the sieved masses. Even with these differences, however, useful comparisons between the two types of measurements can be made with suitable discretion.

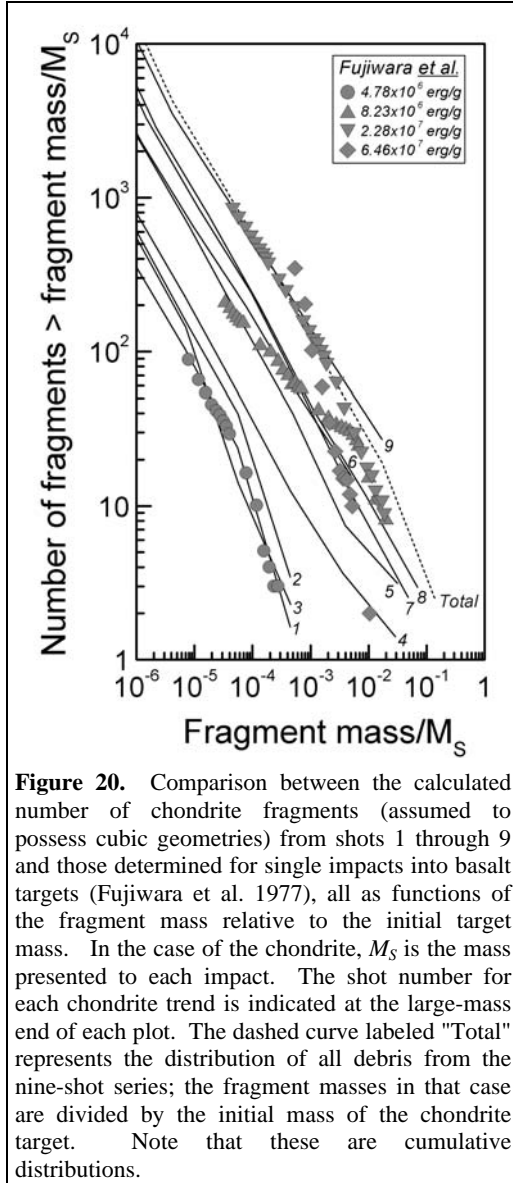


Figure 20. Comparison between the calculated number of chondrite fragments (assumed to possess cubic geometries) from shots 1 through 9 and those determined for single impacts into basalt targets (Fujiwara et al. 1977), all as functions of the fragment mass relative to the initial target mass. In the case of the chondrite, M_s is the mass presented to each impact. The shot number for each chondrite trend is indicated at the large-mass end of each plot. The dashed curve labeled "Total" represents the distribution of all debris from the nine-shot series; the fragment masses in that case are divided by the initial mass of the chondrite target. Note that these are cumulative distributions.

Figure 20 compares the chondrite results with the fragment-number distributions obtained for four basalt targets by Fujiwara et al. (1977), which were impacted by larger, lower-density projectiles (polycarbonate cylinders 8.2 mm in diameter and 6.2 mm in length, with masses of 0.37 g and a density of 1.13 g cm^{-3}) at higher impact speeds (nominally 2.6 km s^{-1}). As was done in Fig. 19, all of the chondrite fragments were assumed to be cubes, so, for the same reasons as given above, the numbers of chondritic fragments in this figure cannot be considered to be absolute. Nevertheless, the overall shapes of the chondrite distributions are invariant with respect to the assumed fragment geometry and, given the resolution differences, the chondritic and basaltic distributions are remarkably similar, with the general shapes of at least three of the four basaltic targets' distributions having close matches in the nine chondrite experiments. While data for the chondrite do not have the resolution to localize with certainty any possible breaks in slope as is typical for such distributions (*e.g.*, Davis and Ryan 1990), the cratering events (chondrite shots 1, 2, and 3) show hints of such structure, with their slopes being similar to those of the three lower-energy impacts in the basalt set, particularly in the upper-mass branches (Table 4).

It is also notable that the energy densities involved in only the last three chondrite experiments were high enough to compare directly with those of the basalts of Fujiwara *et al.*; they possess very little structure compared to those of the basalts. Additionally, the distribution of debris from the most severely disrupted basalt target displays a much higher slope than the fragments from any of the last three chondrite impacts. Indeed, the closest approximation from the chondrite series is found in the steep branch of the distribution from shot 1, which consists of spallation fragments from the vicinity of the impact point. The overall slope of the distribution from the final chondrite impact is much lower than that of the most energetic basalt impact; at a specific energy density of about $1.5 \times 10^7 \text{ erg g}^{-1}$, the last chondrite event falls almost in the middle of the energy-density range of the basalt experiments. Even the distribution of all the debris from the chondrite series possesses a characteristic slope much lower than

Table 4. Slopes of the fits to the various distributions in Figures 20 and 21. The specific energy for the chondrite entries is given relative to the starting mass for each shot in ergs g^{-1} . The slopes b_S and b_L are for the smaller-mass and larger-mass branches of each distribution, respectively. Unlike the case for most of the other targets, there is so little structure in some of the chondrite distributions (the $4.94 \times 10^6 \text{ erg g}^{-1}$ shot, for example) that the assumption of two different slopes can be difficult to justify. The data for the fits listed below were obtained graphically from figures in Fujiwara *et al.* (1977) and Davis and Ryan (1990).

Chondrite			Davis and Ryan											
			Fujiwara et al.			Strong Targets						Weak Targets		
E/M_S	b_S	b_L	E/M_0	b_S	b_L	Aluminum Impactors			Steel Impactors			Aluminum Impactors		
						E/M_0	b_S	b_L	E/M_0	b_S	b_L	E/M_0	b_S	b_L
2.89×10^6	-0.79	-1.29	4.78×10^6	-0.70	-1.46	7.10×10^6	-0.39	-1.47	5.50×10^6	-0.40	-0.89	8.70×10^6	-0.49	-0.84
2.87×10^6	-0.75	-1.17	8.23×10^6	-0.42	-1.05	1.22×10^7	-0.44	-2.62	6.60×10^6	-0.19	-1.08	2.17×10^7	-0.30	-0.81
2.92×10^6	-0.82	-1.00	2.28×10^7	-0.62	-1.01	3.98×10^7	-0.89	-3.00	1.20×10^7	-0.66	-2.24	3.79×10^6	-0.43	-1.21
3.11×10^6	-0.75	-0.52	6.46×10^7	-1.69	-1.81									
2.83×10^6	-0.73	-0.42												
4.11×10^6	-0.72	-0.60												
4.94×10^6	-0.75	-0.73												
7.35×10^6	-0.78	-0.67												
1.52×10^7	-0.76	-0.59												

that from the highest-energy basalt impact. Thus, the fragments from the chondrite were more evenly spread across the range of normalized masses than those from the basalt target, which was relatively depleted in large pieces.

Similar observations can be made (Fig. 21) in comparing the chondrite distributions with those for the mortar targets of Davis and Ryan (1990). The clustering of the mortar data is tighter than that exhibited by the basalt, despite the former incorporating two different strengths. The shapes of most of the size distributions are comparable to those of the chondrite, although some are more complex and some of the smaller-mass branches display much lower slopes than any of the chondrite trends.

In summary, the chondrite number distributions appear to be, overall, little different from those of either the basalt (Fujiwara *et al.*, 1977) or the mortar targets (Davis and Ryan, 1990). Figure 22 plots

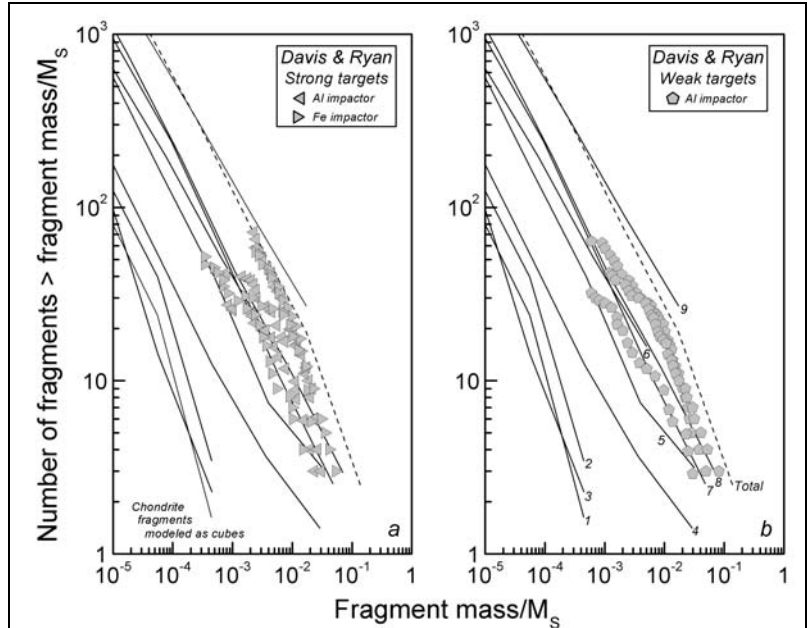


Figure 21. Comparison between the calculated cumulative numbers of chondrite fragments (assumed to possess cubic geometries) and those determined for mortar targets of two different strengths by (Davis and Ryan 1990), all as functions of the fragment mass relative to the initial target mass. Display of the chondrite data is the same as in Fig. 20.

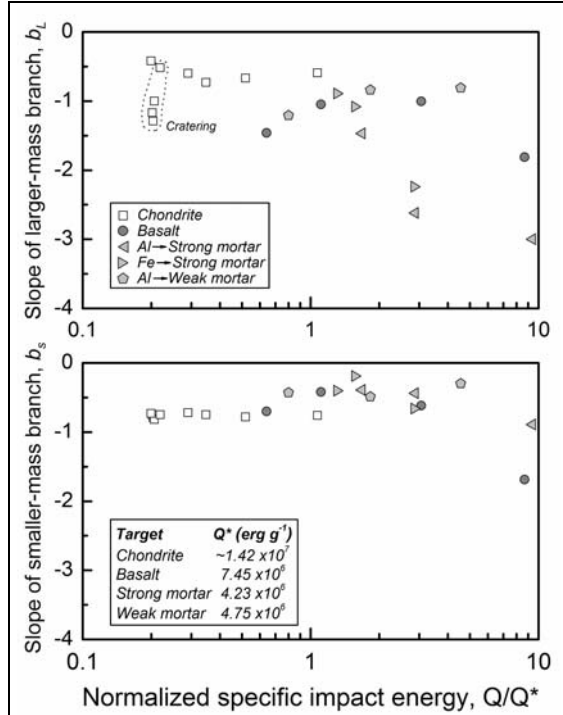


Figure 22. Slopes of the two branches of the number distributions for the chondrite, basalt, and mortar experiments, all vs. the specific impact energy Q normalized to Q^* , the specific impact energy that would result in removal of half the target's mass. The values for the basalt and mortars were derived from the expressions given by Fujiwara *et al.* (1977) and Davis and Ryan (1990), respectively. The value for the chondrite is approximated with the value for anhydrous meteorites given by Flynn and Durda (2004).

the slopes of the two branches of the mass-number distributions for the four targets as functions of the normalized specific impact energy, that is, the specific impact energy Q relative to the specific impact energy required for nominal catastrophic disruption Q^* . (Nominal catastrophic disruption occurs when half the original mass of the target is removed.) Perhaps the most notable feature of the chondrite distributions is the consistency of both slopes over all nine impacts relative to those of the other targets. More markedly than those of the basalt and mortar, the slopes of the smaller-mass branches (b_s) of the chondrite distributions are essentially independent of the normalized specific impact energy and, with few exceptions, the steepest. The slopes of the larger-mass branches (b_L) of the chondrite distributions could be separated into two distinct groups: those from the cratering impacts and the remainder, which represent disruptions of varying degrees. The slopes of the four cratering shots show more variation than the entire group of disruption impacts, a spread that is almost certainly due to

variability in the spallation of large fragments from the irregular target. Values of b_L for the six subsequent impacts, however, are relatively constant and, unlike their lower-mass counterparts, the shallowest of all the targets considered here. Thus, the chondrite typically yielded a greater fraction of very fine particles than the basalt or either of the two mortars at similar specific energies. Conversely, the chondrite broke up more uniformly overall than any of the other targets.

Matsui *et al.* (1982, 1984) determined the distributions of fragment numbers as functions of fragment size from low-velocity, single impacts into basalt, tuff, dunite, and granite targets, documenting the change in slope of the smaller-mass branches of these distributions as the specific impact energy increased. Impact speeds ranged from ~ 47 to 936 m s^{-1} for the basalt and from ~ 17 to 596 m s^{-1} for the tuff, much lower than those of the chondrite series. While the specific impact energies were comparable to those of the chondrite series, those values were attained through use of large impactors of cylindrical steel, from 134 to 497 times more massive than the ceramic spheres used in the chondrite experiments. Thus, the experiments of Matsui *et al.* were, in general, characterized by lower peak stresses (0.7 to 3

GPa) and longer stress-pulse durations. In only one of the tens of experiments was the basalt target as massive as the original chondrite fragment used here, although the remaining masses of chondrite used as the target for shots 8 and 9 were well within the range of target masses used by Matsui et al.

Because it is not straightforward in most cases to choose the point in a given chondrite plot at which a break in slope occurs (should one indeed exist), comparing the chondrite results to the values determined by Matsui et al. is difficult. As addressed above, identification of any change in slope for some of the chondrite experiments can be subjective, so the entire range of sizes from each of the experiments was used in the fitting procedure, except for the three smallest bins. Data for the three smallest bins were not included in the regressions described below. Because they were calculated under the assumption that the final shot of the series was representative of all nine experiments, they display the same slope for the smallest three points in each distribution and would exert a constant bias on each overall slope. Insofar as Matsui et al. (1982, 1984) used incremental

Table 5. Specific energies for the nine shots in the chondrite series, with the corresponding absolute value of the slope of the incremental number vs. size distribution. Uncertainties are given at the 95th percentile.

Shot No.	E/M _s (erg/g)	Slope
1	2.89×10^6	2.38 ± 0.18
2	2.87×10^6	2.25 ± 0.17
3	2.92×10^6	2.58 ± 0.14
4	3.11×10^6	2.26 ± 0.12
5	2.83×10^6	2.20 ± 0.12
6	4.11×10^6	2.06 ± 0.14
7	4.94×10^6	2.20 ± 0.08
8	7.35×10^6	2.16 ± 0.09
9	1.52×10^7	2.01 ± 0.13

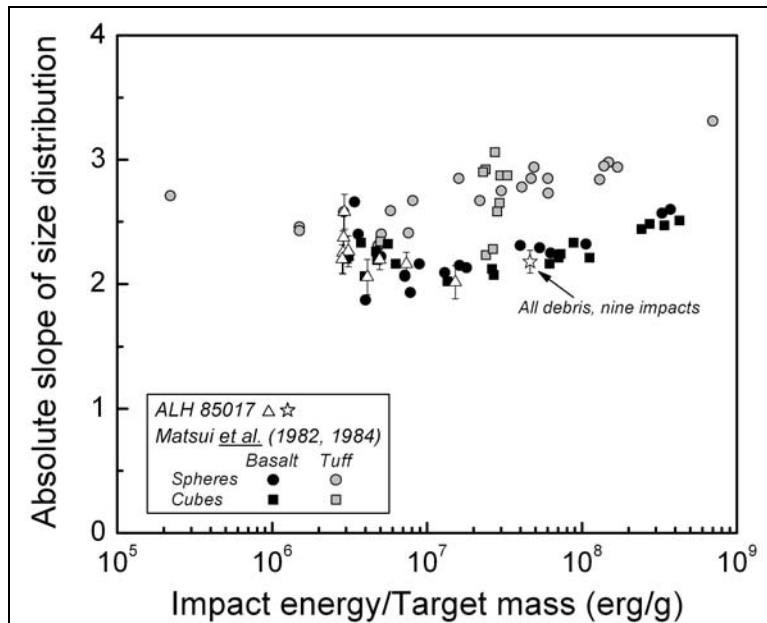


Figure 23. Absolute values of the slopes derived from incremental number vs. specific energy distributions for basalt and tuff targets as determined by Matsui et al. (1982, 1984), along with those from the nine chondrite experiments. Matsui et al. used impactors of steel, basalt, and tuff; only the results from the steel projectiles are used here. Note that the chondrite values fall in the range of the basalt data which, in turn, are mostly distinct from those for the tuff. Uncertainties associated with the chondrite slopes represent 95th percentile limits (Table 5).

number distributions as functions of fragment size, the same is done here, making the slopes here steeper than those in the first part of this section. Note that, in keeping with the convention of Matsui et al., the absolute values of the slopes are given and plotted. Table 5 lists the specific energy for each of the nine shots, along with the absolute values of the derived slopes.

These slope values are shown graphically in Fig. 23, along with the values for the spherical and cubic targets of basalt and tuff as determined by Matsui et al. (1982, 1984). The slopes from the two terrestrial targets compose mostly distinct trends in the

figure, overlapping almost exclusively at their low energy-density ends — locations notorious for pronounced scatter in almost all measures of disruption products. The chondrite points exhibit similar scatter in that range but stay within the limits of the basalt track as the specific energies increase; the total debris from all nine chondrite impacts plotted against the summed specific impact energy provides the point indicated by the star in Fig. 23, which also lies within the basalt trend.

The results of the comparisons in this section are summarized here:

Gabbro — The shapes of the gabbro and chondrite fragment distributions were generally similar, particularly when the final results of each series are compared (*i.e.*, at high specific energies). More large gabbro fragments were created early in both series, a consequence of that material's relative weakness, allowing the onset of disruptive effects much sooner than in the chondrite's case. Conversely, more fines were generated by the chondrite.

Basalts — The basalt targets of Fujiwara et al. (1977) yielded distributions with much better defined breaks in slope in the number-frequency plots than did the chondrite, whose distributions could be described with single slopes while losing little in the precision of the fitted regressions. Nevertheless, there was only one case (the highest-energy impact into one of the basalt targets) that had a slope well outside of the range covered by the chondrite.

The basalt targets of Matsui et al. (1982, 1984), while impacted under conditions that were drastically different from those of the present chondrite series, nevertheless showed slopes that were remarkably similar to those of the chondrite when considered in terms of the specific impact energy.

Mortar — The size distributions of debris from the mortar targets of Davis and Ryan (1990) were more complex than those of the basalts, tuff, gabbro, or chondrite. Typically, the slopes of the small-mass branches were shallower than those of the chondrite, and the large-mass branches were steeper. Except for those from the three cratering impacts, the slopes of the chondrite distributions were much more constant than those from either mortar type.

Tuff — As was noted by Matsui et al. (1982, 1984), the slopes of the fragment distributions for the tuff targets were mostly steeper than those for their basalts. They were also much steeper than those of the chondrite, implying that many more small fragments were created during disruption of the tuff targets. This is not particularly surprising, as the porosity of the tuff would favor rapid decay of stress waves from the impact site, leading to more severe comminution in a smaller volume near the impact point. This effect would be enhanced by the much larger projectiles used in the tuff experiments.

Overall, there is little that is markedly unusual in the shapes of the number distributions from the chondrite impacts when compared to those of the other targets. Perhaps the most obvious characteristic of the chondrite distributions relative to all the others is the almost complete independence of their slopes from the specific impact energy and from the buildup of damage as the impacts accumulated. This could

be attributed to the damage sustained by the meteorite on its parent body and perhaps during their launch and transit to the Earth. If comminution were to proceed by reactivating the myriad, fine-scale fractures, cracks, and other flaws, it is likely that accumulated impact damage would simply further weaken the existing lines and planes of weakness, leading to more debris with size distributions "inherited" from the existing fracture geometries. (This is perhaps a version of the disruption of aggregate targets studied by Ryan et al. 1991.) Greater relative numbers of fine fragments were derived from the chondrite than from any target other than the tuff, and it maintained its integrity to higher specific energies than any of the others. Should a significant fraction of the cosmic-dust complex be derived from ordinary chondrites, models of its generation should consider the apparent ease with which very fine material is created during impacts into (at least L6) ordinary chondrites.

Comments on disruption via multiple impact — In their experimental series designed to simulate the destruction of "cognate tektite" bodies in solar orbit, Gault and Wedekind (1969) examined the responses of solid-glass spheres to single as well as multiple impacts. They found that similar degrees of disruption occurred for a given specific impact energy, whether that energy had been delivered by a single impact or a number of smaller ones (Fig. 24). These general conclusions were later supported by Hörz et al. (1985) with multiple-impact disruption experiments using granodiorite targets. In the latter case, however, about

twice as much specific energy was required to reach the 50%-disruption threshold in the large targets when compared to smaller, single-impact examples. Housen and Holsapple (1999), on the other hand, documented the effect of target dimensions on the single-impact energetics of disruption. By keeping impact speed and the ratio of projectile to target size constant, they demonstrated that large granite targets required less specific energy for a given degree of disruption than did smaller ones. This phenomenon was dictated by the greater number of preexisting flaws (*i.e.*, penetrating fractures, microcracks, etc.) that could be activated in the larger,

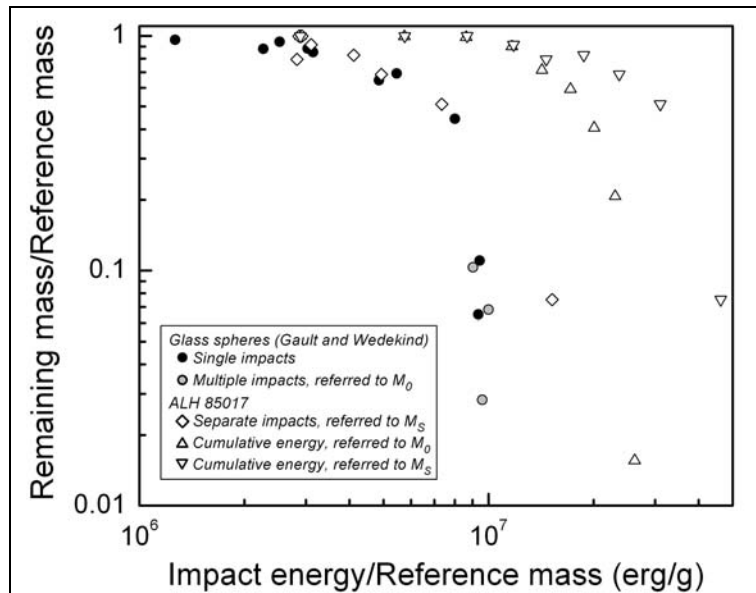


Figure 24. Remaining mass of glass and chondrite targets expressed as fractions of the reference mass as a function of the specific impact energy. The reference masses, depending on the plot, are either the original target mass M_0 or the mass presented to each shot M_S . Each of the three multiple-impact series performed by Gault and Wedekind is represented by a single data point, which depicts the final target configuration at the end of each series. The chondrite plot indicated by the diamonds treats each impact as a separate experiment. See the text for additional details.

more voluminous targets. Thus, their larger targets behaved as if they were weaker than the smaller ones

— the opposite of the granodiorite case. The principal reason for this difference is in the relative size of the impactors: the experiments of Housen and Holsapple purposely scaled the impactors with the targets, so their largest targets had the largest impactors. In the diorite experiments, however, the projectiles were the same regardless of the targets' dimensions. Thus, the initial conditions of the two sets of experiments were very different.

There are additional factors accounting for the difference in disruption energy required by the single- and multiple-impact granodiorite targets. Geometrically, only the earlier events in the multiple-impact experiments occurred normal to the targets' surfaces. Continued spallation and the growing irregularity of the targets' shapes meant that impacts were more likely to be oblique. Since energy and momentum transfer are less efficient at oblique angles (Gault, 1973), the targets required more. In addition, the larger targets meant that the earlier impacts were mostly cratering events. Although the randomly assigned impact locations occasionally produced early spallation of a corner or an edge of the target, most of the impacts simply created craters and displaced far less material than the spallation events (Hörz et al., 1985). The combination of smaller impacts and larger targets placed most of the free surfaces farther from the impact sites and, without proximal free surfaces, spallation was limited. (Not surprisingly, the four-shot granodiorite series had the most energetic individual impacts and yielded a value of $M_R/M_0 \leq 0.5$ at a specific energy more characteristic of single-impact disruptions [Hörz et al., 1985].) Finally, as the impacts accumulated, so did the damage inside the target, leading to a greater density of cracks that could be exploited by the stress waves. Thus, instead of increasing the size of the impactor to encompass more flaws as was the case in the experiments of Housen and Holsapple, the absolute size of the impactors remained unchanged while the targets' flaw densities increased with time. The relentless combination of mounting damage and decreasing target size led to increasingly effective removal of target material.

These observations question the suitability of annealed glass as an analogue material for anything other than the "cognate tektite" bodies that they were intended to represent in the experiments of Gault and Wedekind (1969). Any flaws in the glass would almost certainly be different in nature and geometry from those in natural rocks, perhaps taking the form of bubbles or density differences caused by compositional variations within the glass itself. Because of the homogeneity of the glass, the deep interiors of the spheres could have remained relatively pristine, even after a number of impacts. Without preexisting flaws or gross discontinuities, and given the magnitudes of the impacts, there would have been little physical reason to initiate internal cracking through much of the multiple-impact series. Comparisons between the glass results of Gault and Wedekind (1969) and experiments involving natural rock targets, then, should probably be made only in general terms.

There are no baseline single-impact data for the chondrite, and because of this, interpretation of the results in Fig. 24 is hardly straightforward. When plotted as Gault and Wedekind did for their glass targets, for example, the values of M_R/M_0 for the chondrite as a function of cumulative specific energy take a form very similar in shape to the glass data, but displaced to considerably higher specific energies. Given the similarity between the single-impact data of Gault and Wedekind and the results of their multiple-impact series, then, it would be natural to assume that single-impact results for the chondrite would follow those of the multiple-impact set. No such data are on hand, however, due to the paucity of available chondritic targets (although see the next section). Only the individual experiments that compose this series provide information on the response of ALH 85017 material to single impacts, and using them as points of comparison would invite a serious risk of circular reasoning.

When plotted as individual events, the first eight of the nine chondrite impacts define a trend that is indistinguishable from that of the single-impact glass, which in itself is informative, as the glass used in each experiment was a pristine target. This result is further testimony to the surprising toughness of the crack-ridden ALH 85017, flaws that not only were created by the accumulating damage caused by the impacts in the experimental series, but also those that were intrinsic to the pre-experiment meteorite itself (see Fig. 15, for example). Not surprisingly, then, the last shot of the chondrite series is displaced notably toward higher specific energies than the similarly disrupted glasses. At no point, however, did the single-impact chondrite path approach the chondrite's cumulative-energy trend, contrary to what would be expected on the basis of the glass data. Having noted this result, it would be pointless to speculate further in the absence of independent data.

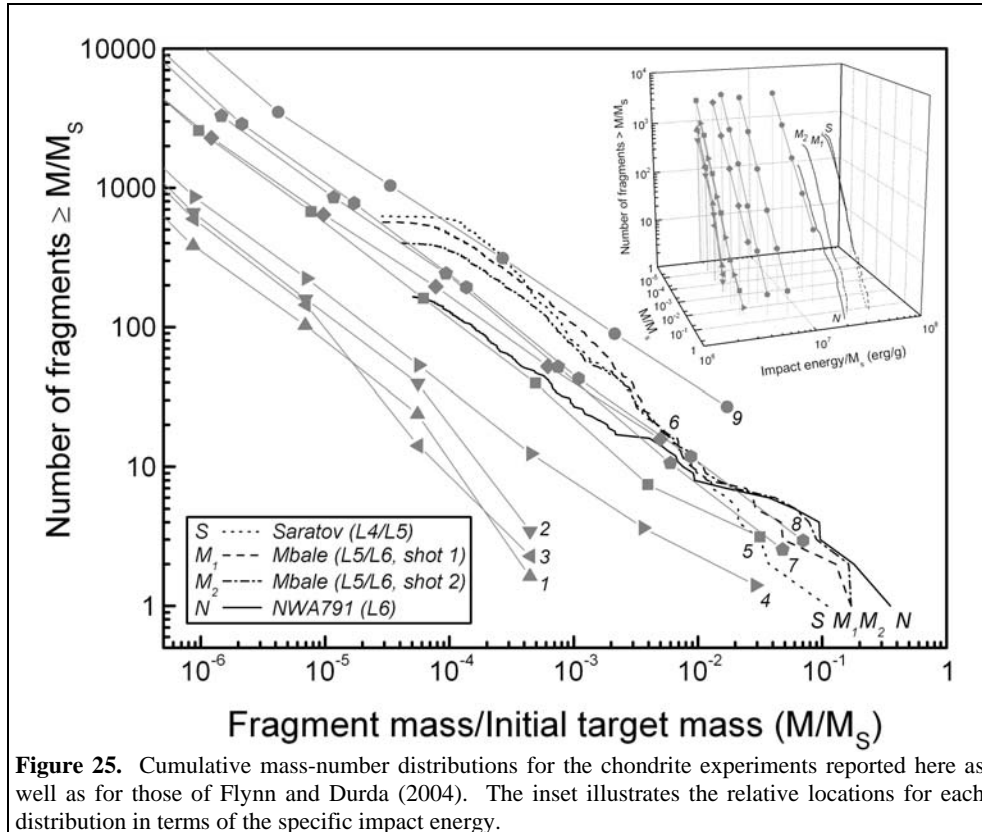
Disruption energetics: ALH 85017 compared to other chondrites — Because meteorites traditionally have been deemed too valuable, their use in disruption and other so-called "destructive" experiments has been rare. The realization that knowledge of the physical properties of meteorites and asteroids is critical to an increased understanding of their origins and histories has led to a growing use of meteorites in such experimentation and testing. Flynn and Durda (2004), for example, used a variety of undifferentiated meteorites in an investigation of potential chemical and mineralogical fractionations in the ejecta from single impacts into those targets. Their experiments also provided data on the disruption behaviors of the meteorites, three of which were L-chondrites; relevant data for four of their experiments are listed in Table 6. (Data for non-L chondrites used by Flynn and Durda can be found in that paper.) The mass-number distributions for the Saratov, Mbale, and NWA791 experiments were determined by weighing and counting individual particles (Flynn and Durda, 2004). Thus, the same caveats as applied to the data from Fujiwara et al. (1977) and Davis and Ryan (1990) are also relevant here. Least-squares fits were made to the smaller-mass branches of the distributions determined by Flynn and Durda; because of the near-continuous nature of their distributions, it is difficult to select break points in those trends, so fits

were made only to the better-defined portions of the small-mass segments. The resulting values for b_S are provided in the final column of Table 6.

Table 6. Meteorites used by Flynn and Durda (2004) and select parameters from their experiments. The impactor in each experiment was an aluminum sphere 3.18 mm in diameter. b_S is the slope fit to the smaller-mass branch of each number-size distribution; a single slope was the best fit to the Saratov data. Mbale, shot 2, was the second impact into that particular fragment, following a low-energy, simple-cratering impact. See Flynn and Durda (2004) for details.

Meteorite	Classification	Mass (g)	Impact speed (km s ⁻¹)	Kinetic energy (erg)	Specific impact energy (erg/g)	b_S
Saratov	L4/L5	105	4.31	4.28×10^9	4.08×10^7	-0.95
Mbale, shot 1	L5/L6	182.5	5.65	7.36×10^9	4.03×10^7	-0.68
Mbale, shot 2	L5/L6	152.4	4.02	3.72×10^9	2.44×10^7	-0.74
NWA791	L6	235.8	4.65	4.98×10^9	2.11×10^7	-0.65

The distributions for the four experiments in Table 6 are shown in Fig. 25 along with those for ALH 85017. Visually, the overall slopes describing three of the single-impact experiments are steeper than those from our nine-shot series. Thus, the single-impact events created debris biased more toward finer fragments, a tendency that appears to be typical of highly energetic, disruptive events and is almost certainly caused by the "overkill" factor, in which the energy densities in the target are so high that few large fragments survive (Gault and Wedekind 1969; Cintala et al. 1984), forcing the slope in plots such as Fig. 25 to be steeper than those from impacts with lower specific energies. It is notable in Fig. 25 that the



slope describing the debris from the lone L6 chondrite in the single-shot experiments of Flynn and Durda was very similar to that for the ninth impact in the ALH 85017 series. Although these two events had similar specific-energy densities, the single-shot results produced some fragments with larger relative masses than did the last of the multiple-impact series, an observation consistent with the description of accumulated damage suggested earlier for the multiple-impact experiments. When allowance is made for the differences between the experimental conditions of Flynn and Durda and those described here, there is nothing to suggest that the behaviors of the targets in the two series were notably dissimilar. Indeed, none of these single-impact experiments shows any indication of the rather dramatic changes in slope that are more typical of the basalt experiments of Fujiwara *et al.* (1977) and the mortar impacts of Davis and Ryan (1990). This suggests that the fragmentation results as described above are not applicable solely to ALH 85017 and could be considered as being representative of L chondrites in general.

Detectability of craters on rock surfaces — Craters formed by high-velocity impacts into rock typically are very shallow and lack raised rims (Hörz *et al.* 1971). Because the spallation surfaces associated with such impacts are broad and irregular, particularly on the surfaces of natural rocks, they can be difficult to recognize; indeed, larger craters on lunar boulders, for instance, often are apparent in photography only when

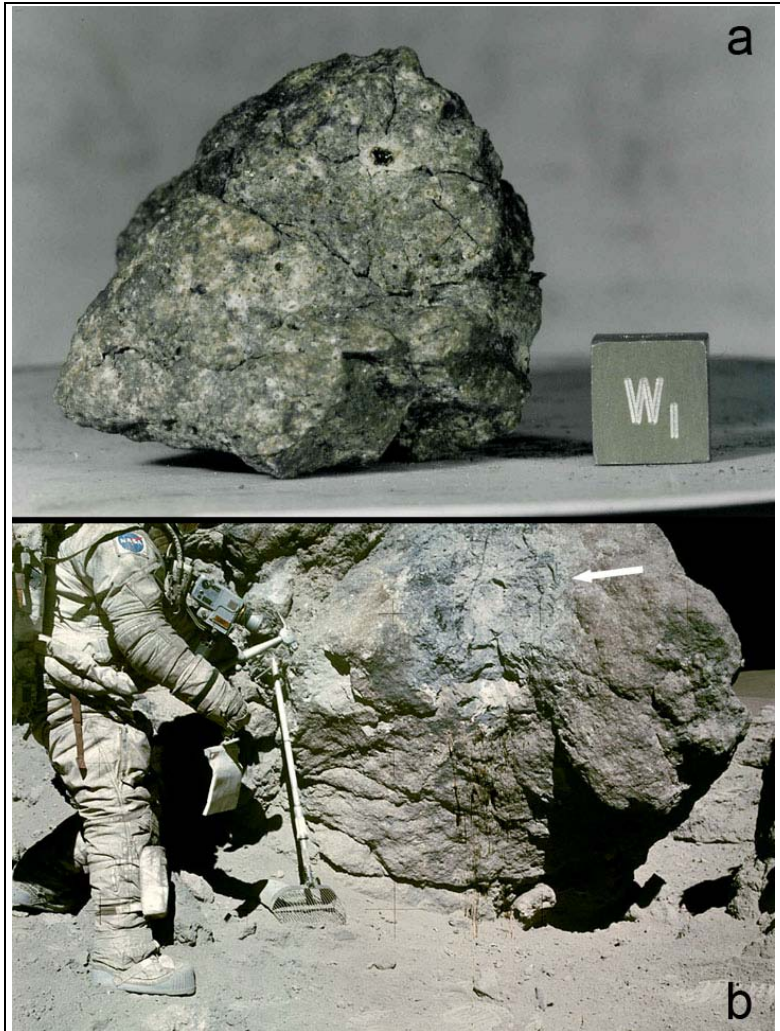


Figure 26. Lunar examples of impact features on rocks, illustrating their less than obvious forms. (a) The dark spot with the bright halo in the upper part of this Apollo 17 breccia (73155) is the central pit of an impact feature. Note the radial cracks extending through the spall zone, which occupies the entire upper half of the rock in this view. NASA photograph 73-17057 (b) Impact crater on Outhouse Rock, Station 11, at the Apollo 16 landing site. The arrow tip is on the edge of the spall zone; the impact point can be located by extending the arrow its own length in the indicated direction. The spall zone from this angle is roughly circular, going clockwise around the crater's center, from about 7:00 to 5:30; from 5:30 to 7:00 it extends almost twice as far from the impact point. NASA photograph AS16-116-18653.

viewed in stereo or otherwise found by careful observation (Figs. 26). (On the other hand, once relatively shallow and non-circular depressions caused by pervasive spallation and removal of local promontories are accepted as evidence for cratering on lunar rocks, most exposed surfaces may be interpreted as hosting a plethora of spall zones.) Given the irregularity of the chondrite's original surfaces, it should then come as no surprise that the craters formed there were less than obvious. Had the crater in Fig. 27 been photographed at even slightly lower resolution or under less suitable lighting conditions, it is doubtful that, without foreknowledge, it would have been recognized as an impact feature. This example might serve as a caveat for those investigators attempting to document craters on planetary or asteroidal

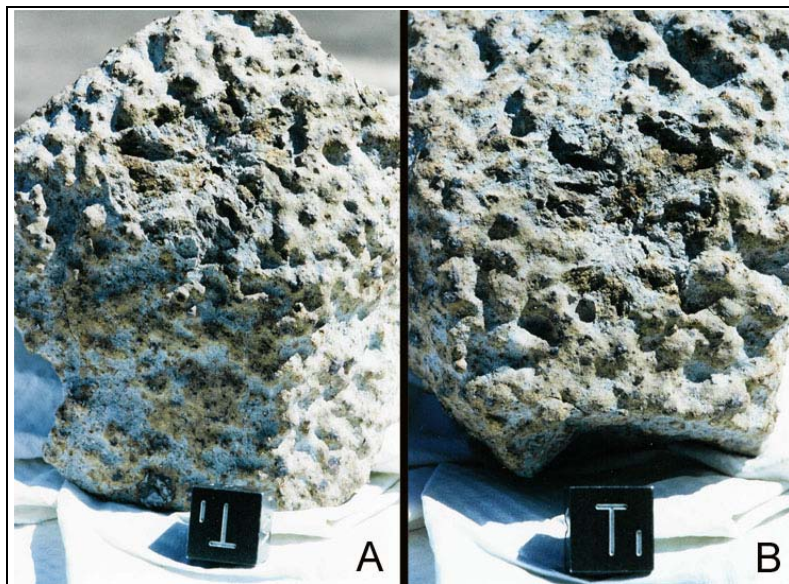


Figure 27. Two views of ALH 85017,13 after the first impact, showing the resulting crater along with the meteorite's post-sandblasting surface morphology. Note the "nodular" appearance of the surface after it was sandblasted; each of the inspected nodules was tipped by a metal grain. Compare this morphology to those of the freshly fractured surfaces in Figs. 1 and 2. (A) The impact point is just left of the centerline of this frame and above the shadowed area dominating the lower left. Most of the impact damage is due to spallation. (B) The same crater illuminated from the opposite direction. Near-grazing illumination was used in each of these photographs to accentuate the crater's relief, illustrating the poorly defined nature typical of impact craters on natural rock surfaces. The cube is 1 cm on a side.

blocks from orbital or even surface photography, in that viewing and lighting geometries as well as photographic resolution would have to be optimal to detect such features. While "zap pits" are common on lunar rocks, they represent only a small, glass-lined interior portion of a much larger spall zone, as illustrated in Fig. 24a. As the diameter of zap pits approaches 1 cm, they are progressively undercut by finely comminuted and displaced material (Hörz *et al.*, 1971), suggesting that they are dislodged entirely during more energetic events. This produces an unremarkable, relatively shallow

spall zone (Fig. 26b), which is further modulated by the detailed, local surface relief, typically resulting in highly irregular and noncircular depressions that are not readily identified as craters. As a consequence, the ostensible absence of craters under less than ideal observing conditions should not be considered as evidence for a lack of hypervelocity impacts.

Conclusions

These experiments should leave little doubt that this particular L6 chondrite has a greater resistance to fragmentation by impact than any of the terrestrial target materials to which it has been compared. Because there are so few data available for comparison, it might be posited that ALH 85017 is

not representative of L6 chondrites in terms of strength. It did, after all, survive removal from its parent body and a prolonged transit time in solar orbit before enduring entry through the Earth's atmosphere, more or less intact. There are, however, no indications that it is a remarkable ordinary chondrite in terms of its petrographic fabric, which, if anything, is hardly pristine (*e.g.*, Fig. 15). ALH 85017 was strong enough to survive ejection and escape from its parent body, but microscopically it was more damaged than either the gabbro or granodiorite targets used for the comparisons made above, both of which could only be described as pristine. Finally, the observations of the chondrite's greater strength relative those of the terrestrial igneous rocks buttresses similar deductions regarding anhydrous meteorites studied by Flynn and Durda (2004) under single-impact conditions. Thus, while these are hardly exhaustive surveys, it is apparent that many meteorites are tougher impact targets than terrestrial stand-ins typically used in experimentation. Indeed, all of the ordinary chondrites used as impact targets — even the relatively porous and friable L4 chondrite Saratov (Flynn and Durda, 2004) — have been, as a group, stronger than their terrestrial proxies. Clearly, the ordinary chondrites are more resistant to impact fragmentation than analogue studies might have assumed.

A marked shortage of fragments in the 63-120 μm range relative to the overall size distribution existed after each of the nine shots into ALH 85017, an observation that is not understood. This appears to have been offset by a decided enhancement in the <63- μm fraction. While calculations indicate that the nature of comminution of crystalline rock is determined by the length of the shock pulse relative to the granularity of the target, the extremely complex, brecciated texture of the chondrite defies a simple, quantitative assessment of its effective grain size and thus of the production of such fine-grained materials. The evolution of surface area created during the comminution of the meteorite indicates that at least one and possibly two enhancements of disruption efficiency occurred during the series of impacts. Such changes were probably related to accumulating damage as well as to the shrinking dimensions of the target as it lost mass, thus facilitating spallation by placing free surfaces closer to the impact point.

Gabbro targets of similar mass and dimensions were weaker than the chondrite, attaining the 50% disruption mark at specific impact energies around 60 to 70% of that needed by the chondrite, in general agreement with single-impact results (Flynn and Durda, 2004). While comparable, the mass vs. grain-size distributions of the comminution products from the gabbro typically possessed shallower slopes than their chondritic counterparts. The chondrite's mass depletion in the 63-120 μm range and enhancement of fines are both starkly apparent when compared to the debris from the gabbro targets. Because more debris was created in the gabbro impacts than in the chondrite experiments, the newly created surface area was higher for the former. By the final shots of the two gabbro series, however, the differences between the gabbro and chondrite were essentially indistinguishable. Further comparisons with multiply-impacted granodiorite targets led to results very similar to those for the gabbro. All three of the diorite targets used

in the comparison were weaker than even the gabbro, and the relative fraction of fines yielded by the diorite also fell well short of those produced by the chondrite.

The overall shapes of the size-number distributions of debris from the chondrite impacts are not unusual when considered in the context of comparable distributions from various targets of natural rock and artificial materials, such as the mortar targets of Davis and Ryan (1990). Nevertheless, the size distributions from ALH 85017 were better behaved than those from the other materials, in that the slopes of the distributions of finer fragments were very consistent throughout the series of impacts. The chondrite was also consistent in its output of the finest debris, which was greater than that of any of the comparison targets. Such a behavior could be due to the preprocessing that the meteorite received on its parent body and possibly during its trip to Earth, with these experimental impacts simply reactivating the damage that already existed. This chondrite was a prolific source of very fine fragments, and it would appear that, through collisions, ordinary chondritic meteoroids are prodigious contributors to the cosmic-dust complex in solar orbit. The shapes of the size-number distributions for debris from L chondrites impacted by Flynn and Durda (2004) are within the range of the distributions from these experiments, indicating that results obtained in both studies probably could be applied to L chondrites in general.

Models of meteoroid survivability that have been founded on the results of the tektite-disruption simulations of Gault and Wedekind (1969) predict lifetimes against collisions that are probably too short. The experiments described above, in conjunction with those of Flynn and Durda (2004), strongly suggest that at least the ordinary chondrites are significantly more resistant to disruption than the glasses of Gault and Wedekind and the basalts, gabbros, and other igneous rocks used as simulated meteoroids and asteroids in disruption experiments.

Finally, by analogy with typical terrestrial igneous rocks, differentiated meteorites could be weaker than ordinary chondrites, leading to the possibility that a strength-dependent selection effect has been operative in the delivery of meteorites to Earth. Not only might ordinary chondrites be better suited than their igneous counterparts to withstand the rigors of survival in the regoliths of their parent bodies and ejection therefrom, but they might also be, by the same token, better able to resist erosion and disruption during the transit to Earth. Should that strength difference also be applicable to the odds of intact passage through the Earth's atmosphere, it would not be surprising if a greater fraction of ordinary chondrites survive to become part of the terrestrial meteorite collection.

Acknowledgements

This work was supported by the NASA Planetary Geology and Geophysics Program, which is acknowledged with no small gratitude. The target meteorite was collected in Antarctica by the Antarctic Search for Meteorites Program under the auspices of the National Science Foundation, sentenced to its

doom by the Meteorite Working Group, and so prepared by the JSC Meteorite Curatorial Staff. The assistance of JSC Curatorial Personnel was instrumental in selecting the fragment of ALH 85017; particular thanks go to Gary "Power Tools" Lofgren for recommendations on the basis of his petrographic reconnaissance as well as for discussions regarding the petrographic textures of ordinary chondrites. The experiments described above were conducted by Frank Cardenas, whose attention to detail, as usual, resulted in high-quality data; Jerry Haynes was equally diligent in constructing an all-plastic set of sieves and the nonmetallic tools used to collect the size-distribution data. Special thanks are due to Dan Durda for providing tabular versions of the data in Figure 25, which saved untold hours of digitizing graphs. Additional discussions with Don Bogard, John Jones, Mark Matney, Duck "David W." Mittlefehldt, and Mike Zolensky were crucial in preventing a nervous breakdown on the part of the senior author. George Flynn and Kevin Housen are hereby recognized for heroic work as they persisted through page after unending manuscript page in their very conscientious reviews of this contribution. The authors are currently attempting to define the dimensionless Housen Number, in which the degree of consternation is somehow inversely proportional to the number of words in a review. Finally, the authors would like to thank Betty Pierazzo for her editorial diplomacy.

Appendix A. One-Dimensional Calculation of Shock-Pulse Thickness

The initial shock pulse generated by an impact into rock will probably never attain the idealized, sharp-edged, spherical shape assumed for purposes of discussion in this and other studies; even if such an ideal shape were to exist early in an event, the random orientations of the target's constituent grains, cracks, flaws, and other inhomogeneities would quickly alter that geometry. As the pulse propagated into the target, it would both weaken and increase in width as consequences of simple, three-dimensional radiation from the impact site and attenuation through the relentless process of rarefaction. Thus, a one-dimensional approximation of the shock's thickness should suffice for the comparisons made in the text. Parts of this derivation can be found, in one form or another, in Gault and Heitowit (1963). Assume that the impactor and target materials each can be described by a linear shock velocity–particle velocity (U - u) relationship, *viz.*,

Table A1. Shock constants for the materials used in this study. Since no such data for ordinary chondrites are known to exist, the values of a and b for the "chondrite" are those for Vacaville basalt. The corresponding values for the ceramic projectiles were determined from data in Marsh (1980). The density for the Bushveldt gabbro was calculated using cylindrical samples of the rock, and its shock velocity–particle velocity relationship was assumed to be the same as that of Frederick diabase (McQueen et al., 1967).

Material	ρ_0 (g cm ⁻³)	a (km s ⁻¹)	b
Ceramic	3.82	6.91	1.44
"Chondrite"	3.22	2.31	1.47
Bushveldt gabbro	2.82	3.78	1.37

$$U_p = a_p + b_p u_p \quad (\text{A1a})$$

and

$$U_t = a_t + b_t u_t \quad (\text{A1b})$$

in which a_x and b_x are material-dependent constants and the p and t subscripts refer to the projectile and target, respectively. Values for the materials in this study are listed in Table A1.

The Rankine-Hugoniot equation for the conservation of momentum gives the stress σ behind a shock front as

$$\sigma - \sigma_0 = \rho_0 U u \quad (\text{A2})$$

in which σ_0 and ρ_0 are the stress and material density, respectively, ahead of the shock front. At the stresses treated here, σ_0 can be ignored with no noticeable effect on the subsequent derivation. Upon impact, the stresses in both the projectile and target materials behind their respective shock fronts are equal in this one-dimensional approximation. Using (A2) for each material, setting the two equations equal, and substituting from (A1a) and (A1b) for U_p and U_t , respectively, gives

$$\rho_{0t} (a_t + b_t u_t) u_t = \rho_{0p} (a_p + b_p u_p) u_p \quad (\text{A3})$$

Because the impactor and target maintain contact at their interface as the shocks propagate, the particle speeds behind the shock in each material must sum to equal the impact speed v_i , or

$$v_i = u_p + u_t \quad (\text{A4})$$

Eq. (A4) can then be used in (A3) to eliminate u_p , giving

$$\rho_{0t}(a_t + b_t u_t)u_t = \rho_{0p}(a_p + b_p[v_i - u_t])(v_i - u_t) \quad (\text{A5a})$$

This is now a quadratic equation in u_t ,

$$(\rho_{0t}b_t - \rho_{0p}b_p)u_t^2 + (\rho_{0t}a_t - \rho_{0p}a_p + 2\rho_{0p}b_p v_i)u_t - \rho_{0p}v_i(a_p + b_p v_i) = 0 \quad (\text{A5b})$$

which can be solved for u_t :

$$u_t = \frac{-(\rho_{0t}a_t - \rho_{0p}a_p + 2\rho_{0p}b_p v_i) \pm \sqrt{(\rho_{0t}a_t - \rho_{0p}a_p + 2\rho_{0p}b_p v_i)^2 + 4\rho_{0p}v_i(\rho_{0t}b_t - \rho_{0p}b_p)(a_p + b_p v_i)}}{2(\rho_{0t}b_t - \rho_{0p}b_p)} \quad (\text{A6})$$

Definition of the conditions determining the choice of the sign before the square root will be left as an exercise for the reader.

Upon contact between the projectile and target, the shock will travel upward into the projectile, compressing it in the process until time τ_c , when its rearward progress is ended by the trailing edge. With l_0 as the thickness of the impactor,

$$\tau_c = \frac{l_0}{U_p} \quad (\text{A7})$$

During this time, the shock front has penetrated a distance d_c into the target (Fig. A1), given by

$$d_c = U_t \tau_c \quad (\text{A8})$$

and the interface between the impactor and target has advanced a distance δ_c past the initial target's surface

$$\delta_c = u_t \tau_c \quad (\text{A9})$$

In this one-dimensional example, however, the target cannot begin its decompression phase until the rarefaction, reflected from the trailing edge, completely traverses the impactor. By the time the rarefaction reaches the projectile-target interface, the shock front will have penetrated the target to a total distance d_f , given by

$$d_f \equiv d_c + d_d = U_t \tau_c + U_t \tau_d = U_t (\tau_c + \tau_d) \quad (\text{A10})$$

where d_d is the distance covered by the shock in the target during the impactor's decompression and τ_d is the time taken to decompress the projectile. In keeping with the spirit of this illustrative example, the speed of the decompressing rarefaction front is taken to equal the shock speed in the uncompressed projectile material. In reality, the rarefaction would travel at the speed of sound in the heated, compressed

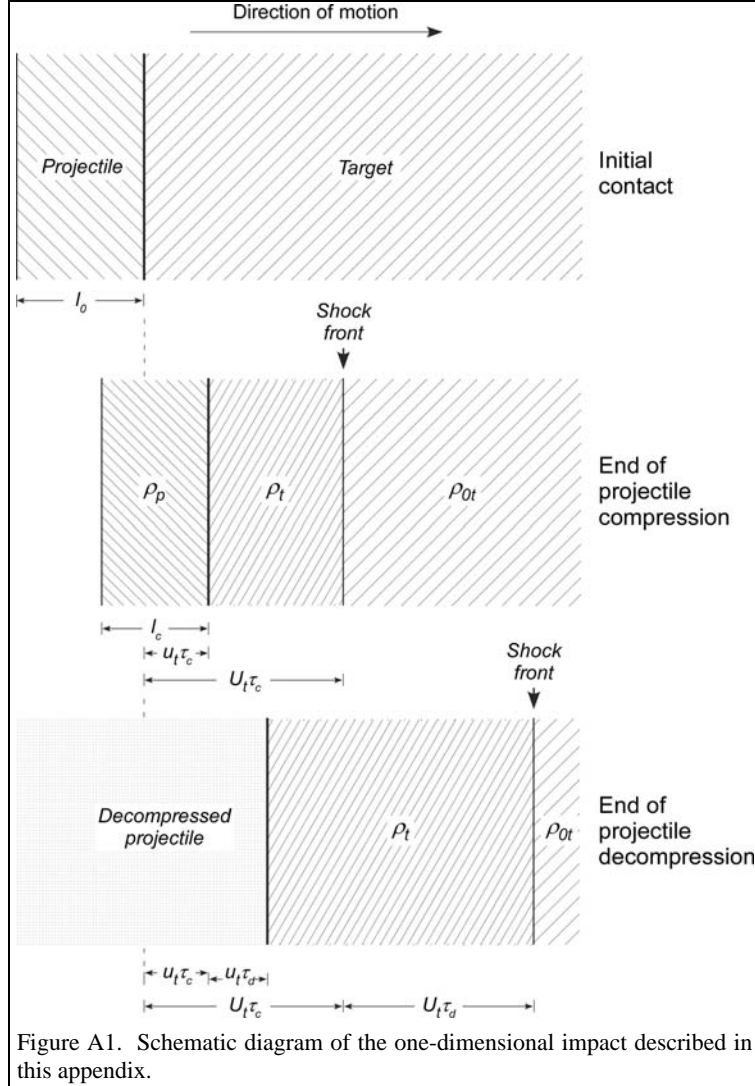


Figure A1. Schematic diagram of the one-dimensional impact described in this appendix.

impactor, which would be greater than U_p (e.g., Melosh, 1989, p.42). Along with other factors as cited below, this assumption should lead to a maximum value for the shock thickness in this example.

By analogy with the compression stage,

$$\tau_d = \frac{l_c}{U_p} \quad (\text{A11})$$

where l_c is the thickness of the compressed impactor at density ρ_p . Conserving the mass of the impactor means that

$$l_0 \rho_{0p} = l_c \rho_p \quad (\text{A12})$$

Furthermore, the Rankine-Hugoniot equation for the conservation of mass during a shock process can be applied to this specific case as

$$\rho_{op} U_p = \rho_p (U_p - u_p) \quad (\text{A13})$$

Combining (A11), (A12), and (A13) then yields

$$\tau_d = \frac{l_0}{U_p} \frac{\rho_{0p}}{\rho_p} = \frac{l_0}{U_p} \left(\frac{U_p - u_p}{U_p} \right) \quad (\text{A14})$$

Applying (A7) and (A14), the total time of travel of the shock front from initial contact through impactor decompression is then

$$\tau_c + \tau_d = \frac{l_o}{U_p} \left[1 + \frac{U_p - u_p}{U_p} \right] = \frac{l_o}{U_p^2} (2U_p - u_p) \quad (\text{A15})$$

At the end of projectile decompression, the shock front has advanced a distance

$$d_f = U_t \frac{l_o}{U_p^2} (2U_p - u_p) \quad (\text{A16})$$

into the target. Following an identical process, the distance traveled by the projectile-target interface during the same time is found to be

$$\delta_f = u_t \frac{l_o}{U_p^2} (2U_p - u_p) \quad (\text{A17})$$

Finally, (A16) and (A17) can be used to give the thickness of the shock in the target as

$$\lambda = (U_t - u_t) \frac{l_o}{U_p^2} (2U_p - u_p) \quad (\text{A18})$$

This is a highly idealized expression for a one-dimensional impact and an assumed decompression front in the compressed projectile that has the same speed as the shock in the impactor. The result is a rectangular shock pulse in the target with thickness λ and amplitude σ , as given by (A2). In reality, the finite geometries and three-dimensional shapes of the impactor and target, geometric attenuation of the shock, entropic losses, and complex wave interactions on the scale of the target texture will produce very different shock profiles (*e.g.*, Melosh, 1984).

Appendix B. Mass-Number and Surface-Area Relationships in Cumulative Mass Distributions

Consider a segment of a cumulative-mass distribution between the masses m_l and m_s , with corresponding particle diameters d_l and d_s (Fig. B1), and assume that the form of the mass distribution between these limits is

$$M = aD^b \quad (\text{B1})$$

Next, assume that the particles in this size range can be assigned a typical shape. The mass of such a particle of density ρ would then be

$$\mu = k \rho D^3 \quad (\text{B2})$$

where k is a geometric constant that depends on the assumed shape; the value of k for a sphere, for instance, would be $\pi/6$.

The differential mass distribution — that is, the mass per diameter increment — can be derived from (B1) by

$$m(D) \equiv \frac{dM}{dD} = abD^{b-1}$$

(B3)

With N as the number of fragments of size D , another way of defining $m(D)$ is

$$m(D) = \mu(D)n(D) \quad (\text{B4})$$

where the differential number distribution is given by

$$n(D) = \frac{dN}{dD} \quad (\text{B5})$$

(B3) and (B4) can then be used to write

$$abD^{b-1} = \mu(D)n(D) \quad (\text{B6})$$

or, using (B2) and rearranging,

$$n(D) = \frac{ab}{k\rho} D^{b-4} \quad (\text{B7})$$

Since $n(D)$ is just the number of fragments per diameter interval, (B7) can be integrated to find

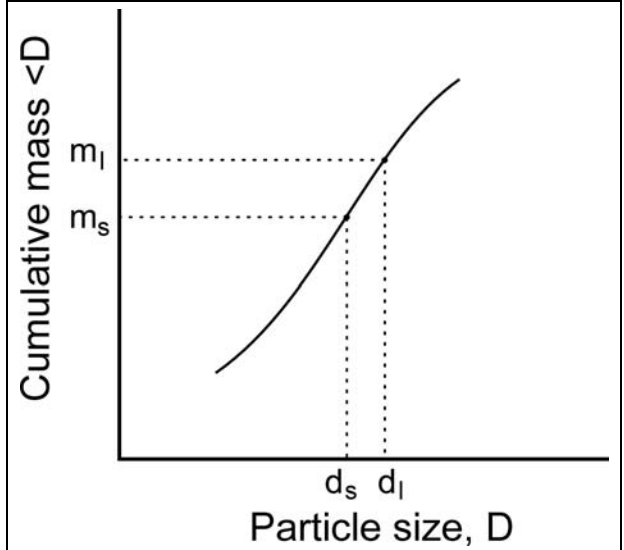


Figure B1. Schematic diagram of a cumulative-mass distribution, illustrating some of the terms used in this appendix.

$$N_{d_1}^{d_2} = \frac{ab}{k\rho} \int_{d_1}^{d_2} D^{b-4} dD = \frac{ab}{k\rho(b-3)} (d_2^{b-3} - d_1^{b-3}) \quad (\text{B8a})$$

In the special case of $b=3$, (B8a) would take the alternate form

$$N_{d_1}^{d_2} = \frac{ab}{k\rho} \int_{d_1}^{d_2} \frac{dD}{D} = \frac{ab}{k\rho} \ln \left(\frac{d_2}{d_1} \right) \quad (\text{B8b})$$

Similarly, the surface area α of a fragment of dimension D can be given by

$$\alpha = k' D^2 \quad (\text{B9})$$

where k' is another geometry-dependent constant; the value for a sphere, for instance, would be π . The differential surface-area distribution $a(D)$ can then be written as

$$a(D) = \alpha(D)n(D) \quad (\text{B10})$$

Using (B7) and (B11) results in

$$a(D) = \frac{k'ab}{k\rho} D^{b-2} \quad (\text{B11})$$

from which the surface area between d_1 and d_2 can be found through

$$A_{d_1}^{d_2} = \frac{k'ab}{k\rho} \int_{d_1}^{d_2} D^{b-2} dD = \frac{k'ab}{k\rho(b-1)} (d_2^{b-1} - d_1^{b-1}) \quad (\text{B12a})$$

or, when $b=1$,

$$A_{d_1}^{d_2} = \frac{k'ab}{k\rho} \int_{d_1}^{d_2} \frac{dD}{D} = \frac{k'ab}{k\rho} \ln \left(\frac{d_2}{d_1} \right) \quad (\text{B12b})$$

In calculating the number and surface-area distributions, a lower size limit of integration d_{min} , below which the cumulative mass is zero, must be determined or defined. Because the exponent in the distribution is determined logarithmically and the mass at or below d_{min} is zero, the final segment is treated linearly. The relationship between the cumulative mass and the fragment size in this smallest size bin can be written as

$$M = \nu D + \beta \quad (\text{B13})$$

from which the slope ν can be found to be

$$\nu = \frac{M - 0}{d - d_{min}} = \frac{M_B}{d - d_{min}} \quad (\text{B14})$$

where M_B is the mass in the smallest bin and d is the upper size-limit of the bin. Because this is a cumulative distribution, the intercept β can then be found from (B13):

$$\beta = M_B - \nu d \quad (\text{B15})$$

Using the same technique as that above to determine the differential mass distribution,

$$m(D) \equiv \frac{dM}{dD} = \nu \quad (\text{B16})$$

Incorporating (B2) and (B4),

$$n(D) = \frac{\nu}{k\rho} D^{-3} \quad (\text{B17})$$

and, integrating (B17) from d_{\min} to d , the number of fragments in the smallest size bin is

$$N_{d_{\min}}^d = \frac{\nu}{2k\rho} (d_{\min}^{-2} - d^{-2}) \quad (\text{B18})$$

Similarly, the differential surface area given in (B10) can be written as

$$a(D) = \frac{k'\nu}{k\rho} D^{-1} \quad (\text{B19})$$

Integration of this expression from d_{\min} to d gives the surface area in the smallest size bin as

$$A_{d_{\min}}^d = \frac{k'\nu}{k\rho} \ln \left(\frac{d}{d_{\min}} \right) \quad (\text{B20})$$

As explained above in **The Data**, the smallest mesh of the custom-made plastic sieve set was 120- μm and the low mass of the target precluded periodic removal of samples from the <120- μm bin, as sampling of quantities sufficient for sieve analyses might have perturbed the evolutionary path of the target during the regolith-evolution phase of the project. At the end (shot 50) of the regolith-evolution phase of the project, however, an adequate sample of the <120- μm fraction was removed and sieved. The results were then assumed to apply to the entire range of both disruption and regolith-evolution experiments, the reasoning for which follows.

Previous "regolith-evolution" experimentation using fragmental gabbro targets (Hörz *et al.* 1984; Cintala and Hörz 1988; Hörz and Cintala 1997) provide data that demonstrate the relative insensitivity of the size distributions in the finest fractions to both impactor dimensions, impact speed (or shock stress), and number of impacts. As a specific example, a comparison among three distinct regolith-evolution experiments involving stainless-steel spheres impacting fragmental gabbro targets demonstrates the consistency of the disruption products in the finest fractions (Fig. B2).

The three different distributions were determined at the ends of the three series described in the figure. Except for the coarsest bin (>44-63 μm), the mass fractions for all three cases are the same within the statistical uncertainty. Only the 200-shot gabbro sample is notably different in the coarsest fraction

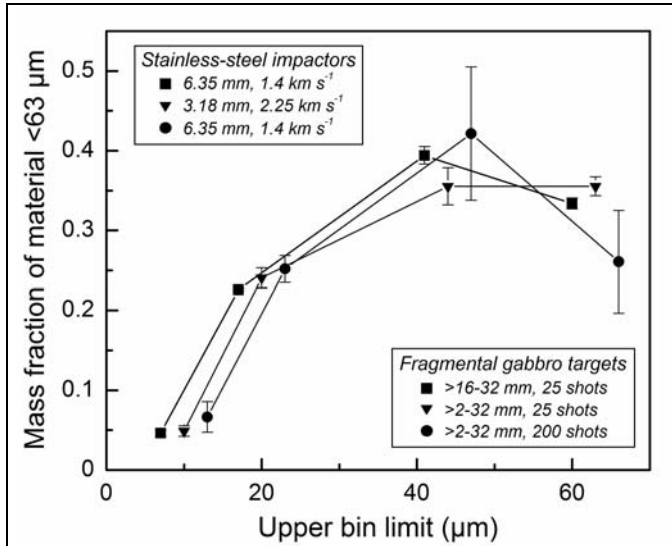


Figure B2. Comparison between the distribution of fines from three regolith-evolution series performed under distinctly different conditions (Hörz *et al.* 1984, Cintala and Hörz 1988; data from the series at 2.25 km s^{-1} have not been published elsewhere). For clarity, the two data sets for the 6.35-mm impactors are plotted to either side of the actual upper bin limit for the relevant size fractions, which are $>44\text{-}63$, $>20\text{-}44$, $>10\text{-}20$, and $<10 \text{ μm}$. The uncertainties represent one standard deviation around the average value as determined from a number of wet-sieving runs. Three samples from the 6.35-mm, 25-shot series, five from the 3.18-mm series, and five from the 200-shot series were sieved.

shown in the figure, and even in that case the other two points almost fall within the $1\text{-}\sigma$ uncertainty of the 200-shot value. (Similar results can be shown for regolith experiments involving dunite and monocrystalline olivine, as well as for anorthositic and monocrystalline albite targets.) Because the targets in both 25-shot series shown in the figure were very coarse-grained relative to the dimensions of the impactors, the individual impacts of those series involved collisions that were more similar to disruption experiments than to impacts into finer-grained "continuum" targets (Cintala and Hörz 1988). We therefore assume that the patterns shown in the generation of fine-grained debris from those 25-shot "disruption" experiments and their similarity to the 200-impact regolith-evolution results have corresponding counterparts in this chondrite

disruption series and the subsequent regolith-evolution experiments.

References

- Asphaug E. E., Ostro S. J., Hudson R. S., Scheeres D. J., and Benz W. 1998. Disruption of kilometre-sized asteroids by energetic collisions. *Nature* 393:437-440.
- Barnouin-Jha O. S., Cintala M. J., and Crawford D. A. 2002. Investigation of the effects of shock duration and grain size on ejecta excavation and crater growth (abstract # 1738). 33rd Lunar and Planetary Science Conference. CD-ROM.
- Britt D. T. and Consolmagno G. J. (2003) Stony meteorite porosities and densities: A review of the data through 2001. *Meteoritics and Planetary Science* 38, 1161-1180.
- Benz W. and Asphaug E. 1994. Impact simulations with fracture: I. Method and tests. *Icarus* 107:98-116.
- Cerroni P. 1986. Simulation of catastrophic fragmentation events: A review of the accelerating techniques and a résumé of the experiments performed until now. *Catastrophic Disruption of Asteroids and Satellites, Mem. Soc. Astron. Ital.* 57:13-45.
- Cheng A. and Barnouin-Jha O.S. 1999. Giant craters on Mathilde. *Icarus* 140:34-48.
- Cintala M. J. and Hörz F. 1984. Catastrophic rupture experiments: Fragment-size analysis and energy considerations (abstract). *Lunar and Planetary Science* XV:158-159.
- Cintala M. J. and Hörz F. 1988. The effects of impact velocity on the evolution of experimental regoliths. *Proceedings, 18th Lunar and Planetary Science Conference*. pp. 409-422.
- Cintala M. J. and Hörz F. 1990. Mineral-dependent comminution during impact cratering (abstract). *Lunar and Planetary Science* XXI:190-191.
- Cintala M. J. and Hörz F. 1992. An experimental evaluation of mineral-specific comminution. *Meteoritics* 27:395-403.
- Cintala M. J., Hörz F., See T. H., Cardenas F., and Thompson T. D. 1984. Regolith evolution experiments I: Grain-size evolution (abstract). *Lunar and Planetary Science* XV:160-161.
- Cintala M. J., Hörz F., See T. H., and Morris R. V. 2004. Generation of an ordinary-chondrite "regolith" by repetitive impact (abstract # 1911). 35th Lunar and Planetary Science Conference. CD-ROM.
- Cintala M. J., Smith S., and Hörz F. 1993. Impact comminution of glasses: Implications for lunar regolith evolution (abstract). *Lunar and Planetary Science* XXIV:293-294.
- Consolmagno G. J. and Britt D. T. 1998. The density and porosity of meteorites from the Vatican collection. *Meteoritics and Planetary Science* 33:1231-1241.
- Consolmagno G. J., Britt D. T. and Stoll C. P. (1998) The porosities of ordinary chondrites: Models and interpretation. *Meteoritics and Planetary Science* 33, 1221-1229.
- Davis D. R. and Ryan E. V. 1990. On collisional disruption: Experimental results and scaling laws. *Icarus* 83:156-182.

Flynn G. J. and Durda D. D. 2004. Chemical and mineralogical size segregation in the impact disruption of inhomogeneous, anhydrous meteorites. *Planetary and Space Science* 52:1129-1140.

Flynn G. J., Moore L. B. and Klöck W. (1999) Density and porosity of stone meteorites: Implications for the density, porosity, cratering, and collisional disruption of asteroids. *Icarus* 142, 97-105.

Fujiwara A. 1980. On the mechanism of catastrophic destruction of minor planets by high-velocity impact. *Icarus* 41:356-364.

Fujiwara A., Kamimoto G., and Tsukamoto A. 1977. Destruction of basaltic bodies by high-velocity impact. *Icarus* 31:277-288.

Fujiwara A., Cerroni P., Davis D.R., Ryan E.V., Di Martino M., Holsapple K.A., and Housen K.R. 1989. Experiments and scaling laws for catastrophic collisions. In *Asteroids II*, edited by Binzel R.P., Gehrels T., and Matthews M.S. Tucson, Arizona: The University of Arizona Press. pp. 240-265.

Gault D.E. (1973) Displaced mass, depth, diameter, and effects of oblique trajectories for impact craters formed in dense crystalline rocks. *The Moon* 6:32-44.

Gault D. E. and Heitowit E. D. 1963. The partition of energy for hypervelocity impact craters formed in rock. Proceedings, 6th Hypervelocity Impact Symposium. pp. 419-456.

Gault D. E. and Wedekind J. A. 1969. The destruction of tektites by micrometeoroid impact. *Journal of Geophysical Research* 74:6780-6794.

Gault D.E., Hörz F., and Hartung J.B. 1972. Effects of microcratering on the lunar surface. Proceedings, 3rd Lunar Science Conference. pp. 2713-2734.

Hörz, F. 1977. Impact cratering and regolith dynamics. *Physics and Chemistry of the Earth* X: 3-15.

Hörz F., Hartung J. B., and Gault D. E. 1971. Microcraters on lunar rocks. *Journal of Geophysical Research* 76:5770-5798.

Hörz F., Gault D. E., and Hartung J. B. 1974. Micrometeoroid abrasion of lunar rocks: A Monte Carlo simulation. Proceedings, 5th Lunar Science Conference. pp. 2397-2412.

Hörz F., Schneider E., Gault D.E., Hartung J.B., Brownlee D.E. 1975. Catastrophic rupture of lunar rocks: A Monte Carlo simulation. *The Moon* 13: 235-258.

Hörz F. and Cintala M. J. 1997. Impact experiments related to the evolution of planetary regoliths. *Meteoritics and Planetary Science* 32:179-209.

Hörz F., Cintala M. J., See T. H., Cardenas F., and Thompson T. D. 1984. Grain size evolution and fractionation trends in an experimental regolith. Proceedings, 15th Lunar and Planetary Science Conference. pp. C183-C196.

Hörz F., Cintala M. J., See T. H., Cardenas F., and Thompson T. D. 1985. Collisional fragmentation of granodiorite targets by multiple impact events (abstract). *Lunar and Planetary Science* XVI:364-365.

Hörz F., Cintala M. J., Bernhard R. P., Cardenas F., Davidson W. E., Haynes G., See T. H., and Winkler J. L. 1995. Penetration Experiments in Aluminum 1100 Targets Using Soda-Lime Glass Projectiles. NASA. NASA TM-104813. 328 p.

- Hörz F., Cintala M. J., See T. H., and Le L. 2005. Shock-melting of ordinary chondrite powders and implications for asteroidal regoliths. *Meteoritics and Planetary Science* 40:1329-1346.
- Housen K. R. and Holsapple K. A. 1990. On the fragmentation of asteroids and planetary satellites. *Icarus* 84:226-253.
- Housen K. R. and Holsapple K. A. 1999. Scale effects in strength-dominated collisions of rocky asteroids. *Icarus* 142:21-33.
- Housen K. R. and Holsapple K. A. 2003. Impact cratering on porous asteroids. *Icarus* 163:102-119.
- Marsh S. P. 1980. LASL Shock Hugoniot Data. Berkeley, CA: University of California Press. 658 p.
- Martelli G., Ryan E. V., Nakamura A. M., and Giblin I. 1994. Catastrophic disruption experiments: recent results. *Planetary and Space Science* 42:1013-1026.
- Matsui T., Waza T., Kani K., and Suzuki S. 1982. Laboratory simulation of planetesimal collision. *Journal of Geophysical Research* 87:10,968-910,982.
- Matsui T., Waza T., and Kani K. 1984. Destruction of rocks by low velocity impact and its implications for accretion and fragmentation processes of planetesimals. Proceedings, 15th Lunar and Planetary Science Conference. pp. B700-B706.
- McQueen R.G., Marsh S.P., and Fritz J.N. 1967. Hugoniot equation of state of twelve rocks. *J. Geophys. Res.* 72: 4999-5036.
- Melosh H.J. 1984. Impact ejection, spallation, and the origin of meteorites. *Icarus* 59: 234-260.
- Melosh H.J. 1989. Impact Cratering: A Geologic Process. New York. Oxford University Press, 245 p.
- Nakamura A., Suguiyama K., and Fujiwara A. 1992 Velocity and spin of fragments from impact disruptions. I. An experimental approach to a general law between mass and velocity. *Icarus* 100:127-135.
- Nakamura A. 1993. Laboratory studies on the velocity of fragments from impact disruptions. Ph.D. thesis, Kyoto University, Kyoto, Japan.
- Oberbeck V. R. 1975. The role of ballistic erosion and sedimentation in lunar stratigraphy. *Reviews of Geophysics and Space Physics* 13:337-362.
- Öpik E. J. 1971. Cratering and the Moon's surface. In *Advances in Astronomy and Astrophysics*, edited by Kopal Z. New York: Academic Press. pp. 108-337.
- Papike J. J., Simon S. B., and Laul J. C. 1982. The lunar regolith: Chemistry, mineralogy, and petrology. *Reviews of Geophysics and Space Physics* 20:761-826.
- Rinehart J.S. 1975. Stress Transients in Solids. Santa Fe, New Mexico: Hyperdynamics. 230 p.
- Rubin S. W., Cintala M. J., and Hörz F. 1991. Collisional-disruption experiments: Analysis of identical impacts (abstract). *Lunar and Planetary Science* XXII:1147-1148.

Ryan E. V., Hartmann W. K., and Davis D. R. 1991. Impact experiments 3: Catastrophic fragmentation of aggregate targets and relation to asteroids. *Icarus* 94:283-298.

Ryan E.V., Davis D.R., and Giblin I. 1999. A laboratory study of simulated Edgeworth-Kuiper Belt objects. *Icarus* 142:56-62.

Wilkison S. L., McCoy T. J., McCamant J. E., Robinson M. S. and Britt D. T. (2003) Porosity and density of ordinary chondrites: Clues to the formation of friable and porous ordinary chondrites. *Meteoritics and Planetary Science* 38, 1533-1546.

Wilkison S. L. and Robinson M. S. (2000) Bulk density of ordinary chondrite meteorites and implications for asteroidal internal structure. *Meteoritics and Planetary Science* 35, 1203-1213.

Yamogida K. and Matsui T. 1983. Physical properties of ordinary chondrites. *Journal of Geophysical Research* 88:9513-9533.